

Contents lists available at ScienceDirect

Journal of the Mechanics and Physics of Solids

journal homepage: www.elsevier.com/locate/jmps





Mechanics of magnetic-shape memory polymers

Lu Lu, Shuai Wu, Ruike Renee Zhao

Department of Mechanical Engineering, Stanford University, Stanford, CA 94305, United States

ARTICLE INFO

Keywords: Magnetic-shape memory polymers Constitutive modeling Finite deformation Shape morphing Shape locking

ABSTRACT

Magnetic-shape memory polymers (M-SMPs) can not only undergo rapid and reversible deformation in response to magnetic actuation but also lock the actuated shape upon cooling, which has great potential in applications such as soft robotics, active metamaterials, and shape-morphing systems. In this work, we develop a constitutive model for M-SMPs with finite deformation. The constitutive model considers the Helmholtz free energy contributed by the thermally responsive shape memory polymers and the magnetically responsive particles, leading to a magneto-thermomechanical framework. It is shown that the developed model can capture the thermomechanical as well as magneto-elastic responses of M-SMPs at different temperatures. Simplified beam models for M-SMPs are presented to show the material's versatile functionalities including fast and reversible deformation, selective/sequential actuation, and shape locking. We envision that the constitutive framework and the simplified beam models presented in this work can serve as useful tools to guide the rational design of M-SMP-based functional structures and devices.

1. Introduction

Magnetic soft materials, comprised of hard-magnetic particles with high coercivity (the resistance to being demagnetized) embedded in polymeric matrices, have attracted significant research attention due to their widespread applications such as soft robotics (Hu et al., 2018; Wang et al., 2021; Wu et al., 2021; Ze et al., 2022), active metamaterials (Chen et al., 2021; Ma et al., 2022; Sim et al., 2023; Sim and Zhao, 2024), and shape morphing structures (Cui et al., 2019; Wang et al., 2023; Leanza et al., 2024). Under the actuation of an applied magnetic field, magnetic soft materials can undergo large deformations, which allows for rapid, untethered, and reversible shape changes and property tunability (Kim et al., 2018; Novelino et al., 2020). However, conventional magnetic soft materials (with inactive polymeric matrices) cannot maintain their actuated shapes once the applied magnetic field is removed. In many practical applications, shape locking after actuation is desired to achieve certain functionality such as load-carrying capability (Ze et al., 2020), selective/sequential actuation (Ma et al., 2021), and reprogrammable shape manipulation (Alapan et al., 2020).

Recently, a magnetic-shape memory polymer (M-SMP) was developed by Ze et al. (2020), where two types of ferromagnetic particles, i.e., Fe₃O₄ and NdFeB, are embedded into thermally responsive shape memory polymers (SMPs) to achieve both shape locking and fast and reversible shape morphing under magnetic field (Ma et al., 2021; Montgomery et al., 2021; Wu et al., 2022). In the M-SMP, the SMP matrix (Zhao et al., 2023a) can memorize the actuated shape in response to temperature change, making it an ideal

E-mail address: rrzhao@stanford.edu (R.R. Zhao).

This paper is dedicated to Prof. Huajian Gao in recognition of his significant contributions to the solid mechanics community and to celebrate his 60th birthday. Ruike Renee Zhao deeply appreciates the invaluable mentorship and support provided by Prof. Gao.

^{*} Corresponding author.

platform for magnetically responsive materials with shape-locking capability. As shown in Fig. 1(a), the M-SMP, in the form of a cantilever beam, contains both Fe_3O_4 and NdFeB particles. The Fe_3O_4 particles can increase their temperature through induction heating under a high-frequency alternating current (AC) magnetic field, and thereby control the temperature of the M-SMP. The NdFeB particles can be magnetized with prescribed magnetization for programmable deformation under magnetic actuation. Thermomechanical properties of M-SMPs with various magnetic particle volume fractions are shown in Fig. 1(b), in which P0-0, P5-15, and P10-15 denote neat-SMP without magnetic particles, M-SMP with 5 vol% Fe_3O_4 and 15 vol% NdFeB, and M-SMP with 10 vol% Fe_3O_4 and 15 vol% NdFeB, respectively (fabrication and characterization details are introduced in Section 3.1). In the initial state, the M-SMP has a high stiffness at low temperatures and cannot deform under the actuation magnetic field. Upon induction heating, the stiffness gradually decreases as the M-SMP turns to the rubbery state from the glassy state. When the temperature reaches the glass transition temperature T_g , the modulus of the M-SMP significantly decreases and thus deforms under the applied actuation magnetic field. After cooling the temperature below T_g , the M-SMP returns to its glassy state, and the actuated configuration can be locked without the need of keeping the external actuation magnetic field. When the M-SMP is reheated above T_g , the deformed state can recover to its initial shape.

By harnessing the magnetically responsive deformation and shape-locking capability, several functional applications have been achieved based on M-SMPs such as shape morphing grippers with high stiffness (Ze et al., 2020) and active metamaterials with tunable properties (Ma et al., 2021; Montgomery et al., 2021; Wu et al., 2022). To enable more functional designs, a comprehensive understanding of the magneto-thermomechanical behavior of M-SMPs is needed. However, the existing constitutive models for hard-magnetic soft materials (Zhao et al., 2019; Stewart and Anand, 2023; Lu et al., 2024) are based on an inactive polymeric matrix, which cannot capture the magneto-thermomechanical behavior of M-SMPs.

The thermomechanical response in M-SMPs is attributed to the glass transition behavior of the SMP matrix. In recent years, various constitutive models have been developed to capture the thermomechanical behavior of SMPs (Nguyen et al., 2008; Qi et al., 2008; Westbrook et al., 2011; Li and Xu, 2011; Xiao et al., 2013; Yu et al., 2016; Li et al., 2017; Zeng et al., 2018; Zeng et al., 2023; Zhao et al., 2023b). For example, Qi et al. (2008) proposed a 3D finite deformation constitutive model by utilizing the concept of phase transitions, which can capture the shape memory effects and shape recovery of SMPs. Xiao et al. (2013) developed a multi-process thermomechanical constitutive model incorporating structural and stress relaxation and examined the effects of temperature and physical aging on the shape memory behavior of amorphous SMPs. Compared to SMPs that have been widely studied, the constitutive model and mechanical behavior of M-SMPs remain unexplored.

In this work, we present a magneto-thermomechanical constitutive model for M-SMPs based on the finite deformation theory. To capture the glass transition in SMPs, the Arruda-Boyce model (Arruda and Boyce, 1993) is applied to describe the behavior in the rubbery state and the neo-Hookean model, along with a nonlinear viscous flow rule, is employed to capture the behavior in the glassy state. In addition, the influence of magnetic particles in response to external magnetic fields is considered using magnetic potential energy. The model is calibrated by fitting the experimental results of dynamic mechanical analysis and uniaxial tensile tests. It is then employed to examine the thermomechanical and magneto-elastic behaviors of M-SMPs at varying temperatures. Further, simplified beam models equipped with the developed constitutive model are presented to show the versatile functionalities of M-SMPs such as rapid and reversible deformation, selective/sequential actuation, and shape locking. It is expected that the reported constitutive model and simplified beam models for M-SMPs can provide guidance for the rational design to achieve functional applications.

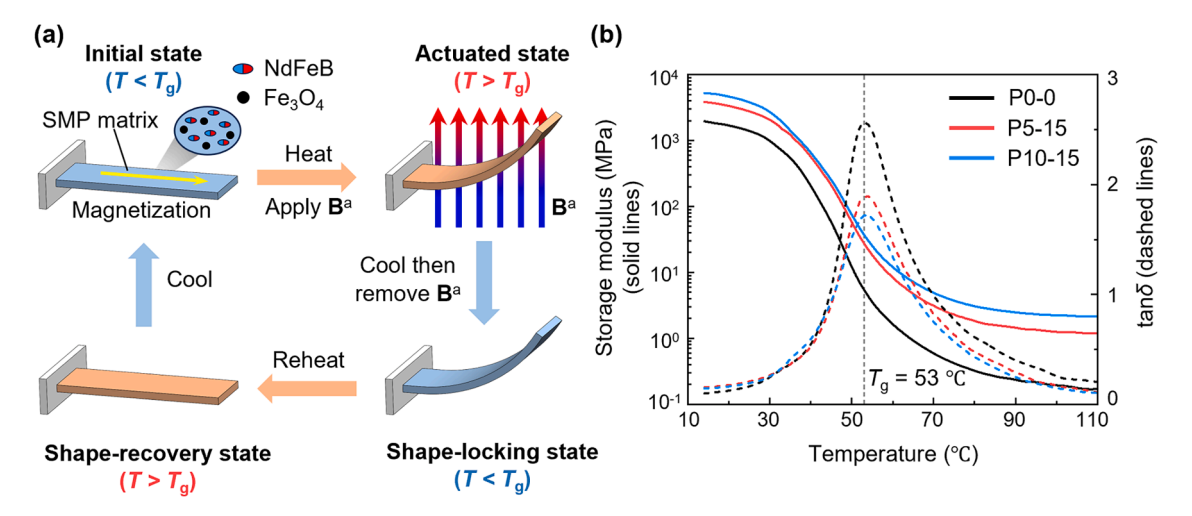


Fig. 1. Working mechanism and thermomechanical properties of magnetic-shape memory polymers (M-SMPs). (a) The M-SMP is fabricated by embedding Fe₃O₄ and NdFeB particles into the SMP matrix. When heating the M-SMP above the glass transition temperature T_g , it can be actuated under an external magnetic field **B**^a. After cooling the M-SMP to room temperature, the actuated shape can be locked without keeping the magnetic field. When reheating the M-SMP above T_g , it automatically recovers to the initial undeformed shape. After cooling, the M-SMP returns to its initial state. (b) Storage moduli and tanδ (the ratio of loss modulus to storage modulus) with respect to temperature for P0-0 neat-SMP, P5-15 M-SMP, and P10-15 M-SMP. The three materials have the same glass transition temperature $T_g = 53$ °C.

The remainder of this paper is organized as follows. In Section 2, a magneto-thermomechanical constitutive model for M-SMPs is developed within the framework of finite deformation theory. In Section 3, we examine the magneto-thermomechanical response of M-SMPs at different temperatures based on the developed constitutive model. In Section 4, the dynamic response of an M-SMP cantilever beam subjected to a uniform time-dependent actuation magnetic field under heating is investigated. In Section 5, the static bending of a two-segment M-SMP beam under a uniform magnetic field and thermal loading is studied. In Section 6, origami structures made of M-SMPs are presented, followed by a summary in Section 7.

2. Constitutive modeling

In this section, we develop a constitutive model to capture the magneto-thermomechanical behavior of M-SMPs within the framework of finite deformation theory.

2.1. Kinematics

The M-SMP is considered as a deformable, isotropic solid continuum body, where the position vectors of a material point in the reference (i.e., undeformed) and current (i.e., deformed) configurations are denoted by **X** and **x**, respectively. The two vectors are related by a smooth deformation map: $\mathbf{x} = \chi(\mathbf{X}, t)$, with t being the time. Then, the deformation gradient is defined by

$$\mathbf{F} = \frac{\partial \chi}{\partial \mathbf{X}},\tag{1}$$

and its Jacobian is denoted by $J = \text{det}(\mathbf{F})$, which characterizes the volume change during the deformation. The deformation gradient can be decomposed multiplicatively into a mechanical component \mathbf{F}_{me} and a thermal component \mathbf{F}_{th} ,

$$\mathbf{F} = \mathbf{F}_{\text{me}} \mathbf{F}_{\text{th}}. \tag{2}$$

To model the thermoviscoelastic behavior of the M-SMP, the mechanical deformation gradient is further decomposed multiplicatively into an elastic component F_e and a viscous component F_v ,

$$\mathbf{F}_{\mathrm{me}} = \mathbf{F}_{\mathrm{e}} \mathbf{F}_{\mathrm{v}}.\tag{3}$$

Since the material is assumed to be isotropic, the thermal deformation gradient can be expressed as

$$\mathbf{F}_{\text{th}} = J_{\text{th}}^{1/3} \mathbf{I},\tag{4}$$

where **I** is the second order identity tensor and $J_{th} = \det(\mathbf{F}_{th})$ is the volume change induced by thermal expansion. When the temperature T is below the glass transition temperature (i.e., $T < T_g$), $J_{th} = 1 + 3\alpha_g(T - T_i)$, where α_g is the linear coefficient of thermal expansion (CTE) of the glassy state and T_i is the initial temperature. When $T > T_g$, $J_{th} = 1 + 3\alpha_r(T - T_i)$, with α_r being the linear CTE of the rubbery state.

Then, the left and right Cauchy-Green deformation tensors for F and its components can be defined as

$$\mathbf{B} = \mathbf{F}\mathbf{F}^{\mathrm{T}}, \mathbf{B}_{\mathrm{me}} = \mathbf{F}_{\mathrm{me}}\mathbf{F}_{\mathrm{me}}^{\mathrm{T}}, \mathbf{B}_{\mathrm{e}} = \mathbf{F}_{\mathrm{e}}\mathbf{F}_{\mathrm{e}}^{\mathrm{T}}, \mathbf{B}_{\mathrm{v}} = \mathbf{F}_{\mathrm{v}}\mathbf{F}_{\mathrm{v}}^{\mathrm{T}},$$

$$\mathbf{C} = \mathbf{F}^{\mathrm{T}}\mathbf{F}, \mathbf{C}_{\mathrm{me}} = \mathbf{F}_{\mathrm{me}}^{\mathrm{T}}\mathbf{F}_{\mathrm{me}}, \mathbf{C}_{\mathrm{e}} = \mathbf{F}_{\mathrm{e}}^{\mathrm{T}}\mathbf{F}_{\mathrm{e}}, \mathbf{C}_{\mathrm{v}} = \mathbf{F}_{\mathrm{v}}^{\mathrm{T}}\mathbf{F}_{\mathrm{v}}.$$

$$(5)$$

Moreover, the remanent magnetization of the M-SMP in the reference and current configurations are denoted by $\widetilde{\mathbf{M}}$ and \mathbf{M} , respectively, and the relationship between them is (Zhao et al., 2019)

$$\mathbf{M} = J^{-1}\mathbf{F}\widetilde{\mathbf{M}}.\tag{6}$$

2.2. Helmholtz free energy density

The total Helmholtz free energy density of the M-SMP can be expressed as

$$\Psi_{\text{total}} = \Psi_{\text{eq}} + \Psi_{\text{neq}} + \Psi_{\text{vol}} + \Psi_{\text{mag}},\tag{7}$$

where the first three terms represent the free energy density of the SMP matrix. Here, Ψ_{eq} and Ψ_{neq} denote the time-independent equilibrium part and time-dependent nonequilibrium part of the deviatoric component, respectively, and Ψ_{vol} represents the volumetric component. The last term, Ψ_{mag} , is the magnetic free energy density of the embedded magnetic particles. The equilibrium part, Ψ_{eq} , describes the hyperelastic behavior of the M-SMP in the rubbery state, which dominates the mechanical response at temperatures above T_g . In the present work, the Arruda-Boyce eight-chain model (Arruda and Boyce, 1993) is applied to capture the rubbery response, which gives

$$\Psi_{\rm eq} = \mu_{\rm N} \lambda_{\rm L}^2 \left[\frac{\overline{\lambda}_{\rm eff}}{\lambda_{\rm L}} \beta + \ln \left(\frac{\beta}{\sinh \beta} \right) \right] - w_0, \tag{8}$$

where $\mu_{\rm N}$ is the characteristic stiffness of the polymeric network and $\lambda_{\rm L}$ is the locking stretch. $\overline{\lambda}_{\rm eff} = \sqrt{\overline{I}_{\rm me1}}/3$ is the effective chain stretch of the network, with $\overline{I}_{\rm me1} = {\rm tr}(\overline{\bf B}_{\rm me})$ being the first invariant of $\overline{\bf B}_{\rm me}$ and $\overline{\bf B}_{\rm me} = J_{\rm me}^{-2/3}{\bf B}_{\rm me}$ being the deviatoric part of ${\bf B}_{\rm me}$. Moreover, $\beta = \mathcal{L}^{-1}(\overline{\lambda}_{\rm eff}/\lambda_{\rm L})$ is the inverse Langevin function with $\mathcal{L}(x) = {\rm coth}x - 1/x$, and w_0 is a constant associated with the energy of the undeformed chain.

The nonequilibrium part, Ψ_{neq} , captures the behavior of the M-SMP in the glassy state, which plays a dominant role at temperatures below T_{e} , and can be evaluated by the neo-Hookean model, as

$$\Psi_{\text{neq}} = \frac{\mu_{\text{neq}}}{2} (\bar{I}_{e1} - 3),$$
 (9)

where μ_{neq} is the shear modulus of the nonequilibrium component, and $\overline{I}_{e1} = \text{tr}(\overline{\mathbf{B}}_e)$ is the first invariant of $\overline{\mathbf{B}}_e$ with $\overline{\mathbf{B}}_e = J_e^{-2/3}\mathbf{B}_e$ being the deviatoric part of \mathbf{B}_e .

Moreover, the Helmholtz free energy density of the volumetric component is considered to be (Nguyen et al., 2008)

$$\Psi_{\text{vol}} = K(J_{\text{me}} - \ln J_{\text{me}} - 1),$$
 (10)

where K is the bulk modulus.

Finally, the magnetic Helmholtz free energy density in the reference state can be expressed as (Zhao et al., 2019)

$$\Psi_{\text{mag}} = -\mathbf{F}\widetilde{\mathbf{M}} \cdot \mathbf{B}^{\text{a}},\tag{11}$$

where **B**^a is the applied actuation magnetic field.

2.3. Stress-strain relation

With the Helmholtz free energy density, the second Piola-Kirchhoff stress can be obtained as

$$\mathbf{S} = 2\frac{\partial \Psi_{\text{total}}}{\partial \mathbf{C}} = 2\frac{\partial \Psi_{\text{eq}}}{\partial \mathbf{C}} + 2\frac{\partial \Psi_{\text{neq}}}{\partial \mathbf{C}} + 2\frac{\partial \Psi_{\text{vol}}}{\partial \mathbf{C}} + 2\frac{\partial \Psi_{\text{mag}}}{\partial \mathbf{C}}.$$
(12)

Substituting Eqs. (8)–(11) into Eq. (12) yields

$$\mathbf{S} = \underbrace{\mu_{\mathrm{N}} J_{\mathrm{me}}^{-2/3} \frac{\lambda_{\mathrm{L}}}{3\overline{\lambda}_{\mathrm{eff}}} \mathscr{L}^{-1} \left(\frac{\overline{\lambda}_{\mathrm{eff}}}{\lambda_{\mathrm{L}}} \right) \left(\mathbf{F}^{-1} \mathbf{F}_{\mathrm{me}} \mathbf{F}_{\mathrm{me}}^{\mathrm{T}} \mathbf{F}^{-\mathrm{T}} - \frac{1}{3} I_{\mathrm{me1}} \mathbf{C}^{-1} \right)}_{\mathbf{S}_{\mathrm{eq}}} + \underbrace{\mu_{\mathrm{neq}} J_{\mathrm{e}}^{-2/3} \left(\mathbf{F}^{-1} \mathbf{F}_{\mathrm{e}} \mathbf{F}_{\mathrm{e}}^{\mathrm{T}} \mathbf{F}^{-\mathrm{T}} - \frac{1}{3} I_{\mathrm{e1}} \mathbf{C}^{-1} \right)}_{\mathbf{S}_{\mathrm{neq}}} + \underbrace{K(J_{\mathrm{me}} - 1) \mathbf{C}^{-1}}_{\mathbf{S}_{\mathrm{was}}} + \underbrace{\left(-\mathbf{F}^{-1} \mathbf{B}^{\mathrm{a}} \otimes \widetilde{\mathbf{M}} \right)}_{\mathbf{S}_{\mathrm{mea}}}, \tag{13}$$

where the operation \otimes represents the dyadic product that turns two vectors into a second-order tensor. By using the Piola transformation,

$$\sigma = J^{-1} \mathbf{F} \mathbf{S} \mathbf{F}^{\mathrm{T}} = J^{-1} \mathbf{F} \mathbf{S}_{\mathrm{eq}} \mathbf{F}^{\mathrm{T}} + J^{-1} \mathbf{F} \mathbf{S}_{\mathrm{neq}} \mathbf{F}^{\mathrm{T}} + J^{-1} \mathbf{F} \mathbf{S}_{\mathrm{mag}} \mathbf{F}^{\mathrm{T}}, \tag{14}$$

the Cauchy stress can be obtained as

$$\sigma = \underbrace{\frac{\mu_{\text{N}}}{3J} \frac{\lambda_{\text{L}}}{\bar{\lambda}_{\text{eff}}} \mathscr{L}^{-1} \left(\frac{\bar{\lambda}_{\text{eff}}}{\lambda_{\text{L}}} \right) \left(\overline{\mathbf{B}}_{\text{me}} - \frac{1}{3} \overline{I}_{\text{mel}} \mathbf{I} \right)}_{\sigma_{\text{neq}}} + \underbrace{\frac{\mu_{\text{neq}}}{J} \left(\overline{\mathbf{B}}_{\text{e}} - \frac{1}{3} \overline{I}_{\text{el}} \mathbf{I} \right)}_{\sigma_{\text{neq}}} + \underbrace{\frac{K}{J} (J_{\text{me}} - 1) \mathbf{I}}_{\sigma_{\text{vol}}} + \underbrace{(-\mathbf{B}^{\text{a}} \otimes \mathbf{M})}_{\sigma_{\text{mag}}}.$$
(15)

2.4. Viscous flow rule

It is seen from Eq. (15) that the total Cauchy stress of the M-SMP depends on the mechanical left Cauchy-Green tensor B_{me} as well as its elastic component B_e . The evolution of B_e is determined using the following viscous flow rule (Boyce et al., 1988; Qi et al., 2008; Li and Xu, 2011),

$$\mathbf{D}_{\mathbf{v}} = \dot{\gamma}_{\mathbf{v}} \mathbf{n},\tag{16}$$

where $\mathbf{D}_v = \text{sym}(\hat{\mathbf{F}}_v \mathbf{F}_v^{-1})$ is the symmetric part of the viscous velocity gradient with $\mathbf{F}_v = \mathbf{F}_e^{-1} \mathbf{F}_{me}$, and $\mathbf{n} = \vec{\sigma}_{neq} / \| \vec{\sigma}_{neq} \|$ is the normalized deviatoric part of the nonequilibrium component of the Cauchy stress with $\vec{\sigma}_{neq} = \sigma_{neq} - \text{tr}(\sigma_{neq})\mathbf{I}/3$, representing the direction of the viscous flow. Moreover, $\dot{\gamma}_v$ is the shear strain rate, which is described by the Eyring model (Eyring, 1936) with the temperature dependence following the Williams-Landel-Ferry (WLF) kinetics (Ferry, 1980) as

$$\dot{\gamma}_{v} = \frac{s_{y}}{\sqrt{2}\eta_{z}} \frac{T}{Q_{s}} \exp\left[\frac{C_{1}^{g}}{\log e} \left(\frac{T - T_{g}}{C_{2}^{g} + T - T_{g}}\right)\right] \sinh\left(\frac{Q_{s}\overline{\tau}}{Ts_{v}}\right). \tag{17}$$

Here, C_1^g and C_2^g are the two WLF constants at the glass transition temperature, which can be determined from the dynamic mechanical analysis for the storage modulus. η_s is the characteristic shear viscosity, Q_s is the activation parameter for viscous flow, $\bar{\tau} = \|\vec{\sigma}_{\text{neq}}\|/\sqrt{2}$ is the equivalent shear stress, and s_y is the yield strength. The yield strength is assumed to obey the phenomenological evolution rule proposed by Boyce et al. (1989), which gives

$$\dot{s}_{y} = h_0 \left(1 - \frac{s_{y}}{s_{s}} \dot{\gamma}_{v}, \right) \tag{18}$$

with $s_v(0) = s_0$, where s_0 is the initial yield strength and s_s is the steady-state yield strength, and h_0 is flow softening modulus.

3. Magneto-thermomechanical response of M-SMPs

In this section, the ability of the constitutive model to predict the magneto-thermomechanical behavior of M-SMPs will be demonstrated. First, we fabricate neat-SMP and M-SMPs with various volume contents of magnetic particles and characterize their thermal and mechanical properties. Also, we conduct isothermal uniaxial tensile tests to obtain their stress-strain curves at different temperatures. Then, the parameters in the constitutive model are calibrated by curve fitting, after which the model is used to predict the magneto-thermomechanical behavior of M-SMPs.

3.1. Fabrication and thermomechanical characterization of M-SMPs

The M-SMP used in this work is an arylate-based amorphous polymer matrix consisting of two types of magnetic particles, i.e., Fe_3O_4 (100 nm, US Research Nanomaterials, Inc., USA) and NdFeB (25 μ m, Magnequench, Singapore). The P5-15, P10-15, and P0-30

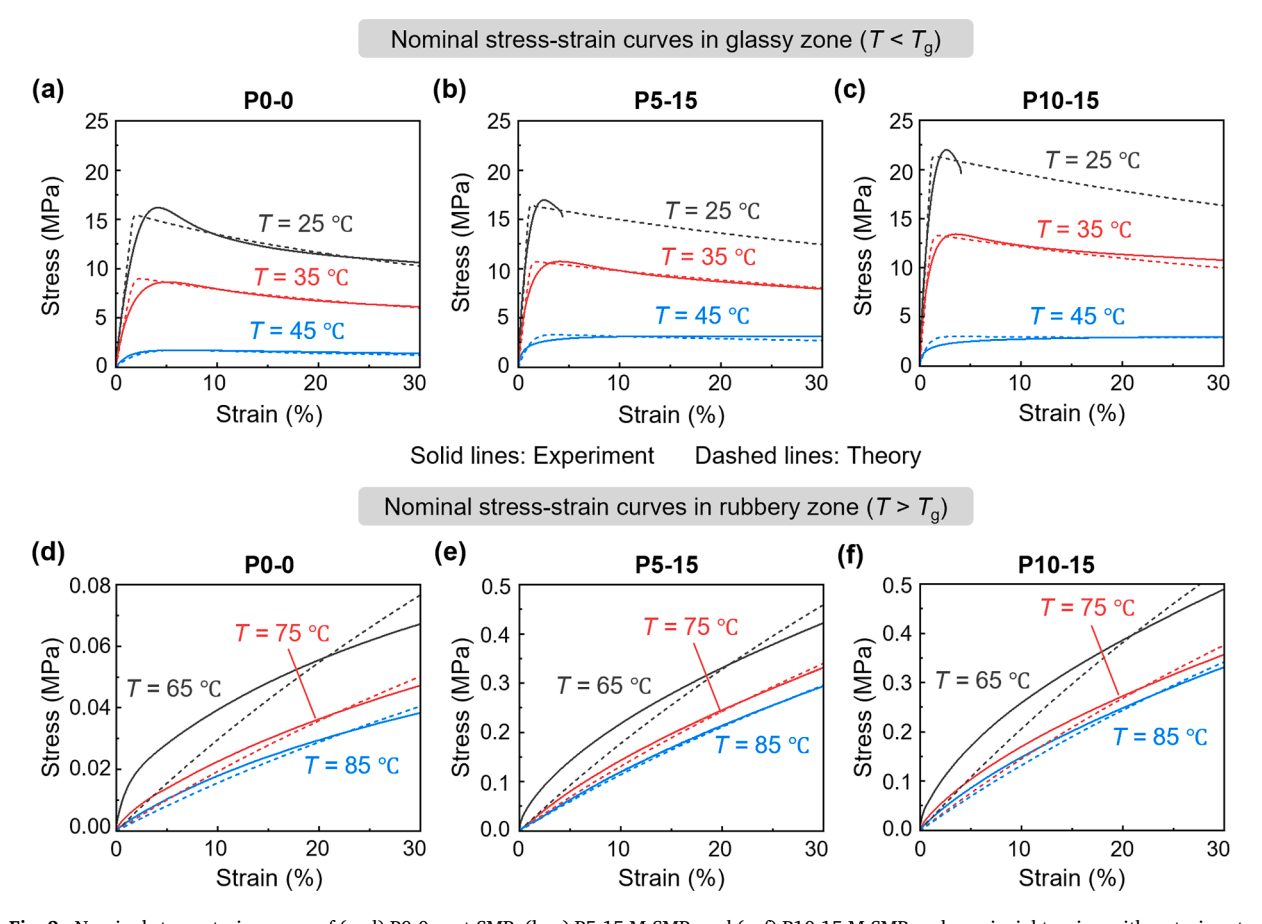


Fig. 2. Nominal stress-strain curves of (a, d) P0-0 neat-SMP, (b, e) P5-15 M-SMP, and (c, f) P10-15 M-SMP under uniaxial tension with a strain rate 0.01 s^{-1} at different temperatures. Solid lines represent the results obtained by experiments, and dashed lines denote the results evaluated by the constitutive model.

M-SMPs are fabricated by mixing the neat-SMP resin with Fe_3O_4 and NdFeB particles in volume ratios of 80:5:15, 75:10:15, 70:0:30, respectively. The neat-SMP and M-SMPs are thermally cured at 80 °C for 7 hours before use. More details on the composite fabrication can be found in Section S1 in Supplementary Material.

A dynamic mechanical analyzer, DMA850 (TA Instruments, USA), is utilized for the thermomechanical and uniaxial tensile tests of M-SMPs. First, the glass transition behavior of the neat-SMP, P5-15 M-SMP, and P10-15 M-SMP is characterized, and the results are shown in Fig. 1(b). In the experiments, the temperature sweeps from 10 °C to 120 °C. After reaching thermal equilibrium, specimens (20 mm \times 5 mm \times 2 mm for neat-SMP and 20 mm \times 2 mm \times 0.75 mm for M-SMPs) are oscillated at 1 Hz with an amplitude of 0.1% strain to obtain the storage modulus and loss modulus. The glass transition temperature, corresponding to the peak temperature of the loss tangent (tan δ) curve, is identified as 53 °C for the three materials. Around the glass transition temperature, the storage moduli of both neat-SMP and M-SMPs drop dramatically by almost three orders of magnitude.

Then, isothermal uniaxial tensile tests are conducted for the neat-SMP, P5-15 M-SMP, and P10-15 M-SMP. In the tests, a preload of 5×10^{-3} N is first applied to straighten the specimens. The dimensions of the specimens are 20 mm \times 2 mm \times 0.75 mm for tests below 40 °C and 20 mm \times 4 mm \times 0.75 mm for the others. After reaching thermal equilibrium, the specimens are stretched at a strain rate of 0.01 s⁻¹ to obtain the stress-strain curves, and the results are shown in Fig. 2.

3.2. Thermomechanical response

Under uniaxial tension, the nominal stress and viscous flow rule of a nearly incompressible M-SMP are derived in **Appendices A** and **B**, respectively, which are then implemented into a MATLAB script to fit the experimental results and calibrate the unknown material parameters in the constitutive model. Details on how to identify these parameters are provided in Section S2 and Figs. S1–S3 in Supplementary Material, and the calibrated material parameters for the neat-SMP and the two types of M-SMPs are presented in Table 1. Fig. 2 compares the nominal stress-strain curves of the neat-SMP and M-SMPs predicted by the constitutive model with those obtained from experiments at different temperatures. It is seen that in the glassy zone (i.e., $T < T_g$), as shown in Fig. 2(a–c), the theoretical predictions agree well with the experimental results for various temperatures and magnetic particle volume fractions. At temperatures (e.g., 25 °C and 35 °C) much lower than T_g , the glassy behavior dominates in the SMPs. In this situation, both the neat-SMP and the M-SMPs exhibit softening behavior after reaching the yielding point. Due to the embedded magnetic particles, M-SMPs become brittle at room temperature and break at a tensile strain of about 3%. As the temperature increases, the SMPs gradually transition into the rubbery state, and the yielding behavior diminishes. When $T > T_g$, both the neat-SMP and M-SMPs exhibit rubbery behavior, with the stress nonlinearly increasing with the strain, as shown in Fig. 2(d–f). One can see that the developed model can also reasonably predict the rubbery stress-strain response for the three materials at high temperatures.

3.3. Magneto-elastic response

When the temperature of the M-SMP is above the glass transition temperature $T_{\rm g}$, the M-SMP enters the rubbery state with a significantly reduced modulus, allowing it to deform under the actuation magnetic fields. To demonstrate the ability of the constitutive model in capturing the magneto-elastic response of M-SMPs, we consider a cubic solid made of M-SMPs subjected to a uniform magnetic field aligned with its magnetization direction, as shown in Fig. 3(a). Relationship between the magnetic field and the stretch ratio of a cube under uniaxial magnetic field is derived in **Appendix C**. Fig. 3(b) and 3(c) show the mechanical stretch ratio as a function of the normalized magnetic field for P5-15 M-SMP and P10-15 M-SMP, respectively. It is seen that when the magnetic field is aligned with the magnetization (i.e., $|\mathbf{M}||\mathbf{B}^a|/\mu_{\rm N}>0$), stretching (i.e., $\lambda_{\rm me}>1$) is induced along the direction of the magnetization. In contrast, when the magnetic field is opposite to the magnetization (i.e., $|\mathbf{M}||\mathbf{B}^a|/\mu_{\rm N}<0$), contraction (i.e., $\lambda_{\rm me}<1$) is induced. Moreover, as the temperature increases, the elastic modulus of the M-SMP decreases, resulting in larger deformations induced by the magnetic field.

Table 1Material parameters in the constitutive model for neat-SMP and M-SMPs.

Material parameters	P0-0 neat-SMP	P5-15 M-SMP	P10-15 M-SMP	Physical meaning of the material parameters
$\alpha_{\rm r}$ (°C ⁻¹)	2.62×10 ⁻⁴	1.45×10 ⁻⁴	1.32×10 ⁻⁴	Linear CTE of the rubbery state
a_{g} (°C ⁻¹)	2.03×10^{-4}	1.32×10^{-4}	1.30×10^{-4}	Linear CTE of the glassy state
Tg (°C)	53	53	53	Glass transition temperature
$\lambda_{ m L}$	4.12	4.12	4.12	Locking stretch
s_0 (MPa)	16	17	22	Initial yield strength
s_s (MPa)	11.6	13.6	20.9	Steady-state yield strength
Q _s (°C)	729.9	754.4	553.4	Activation parameter for viscous flow
h_0 (MPa)	29.56	2.77	1.00	Flow softening modulus
η _s (MPa•s)	3.16	6.46	7.72	Characteristic shear viscosity
$C_1^{\rm g}$	9.13	11.31	9.48	First WLF constant
C_2^{g} (°C)	60.23	68.59	71.87	Second WLF constant

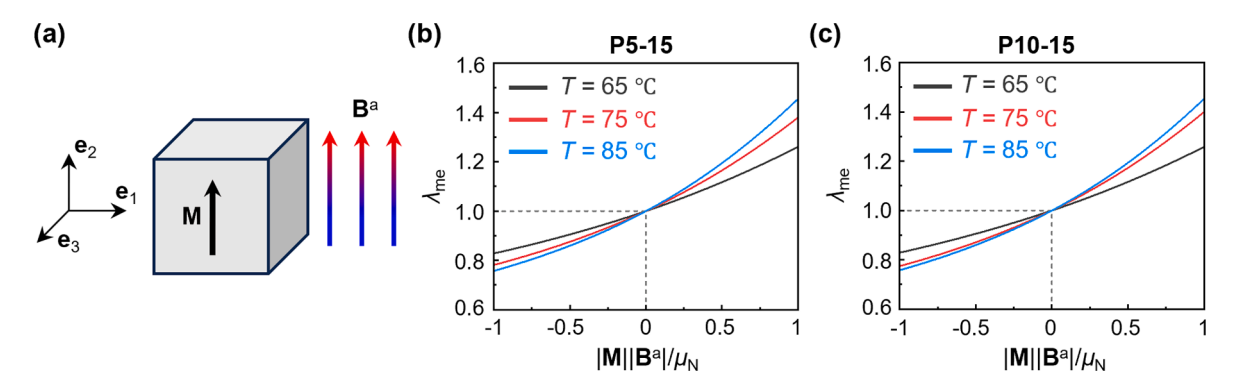


Fig. 3. Uniaxial magnetic actuation of an M-SMP cubic solid. (a) Schematic of a cube subjected to a uniform magnetic field \mathbf{B}^a aligned with its magnetization \mathbf{M} . (b) Mechanical stretch ratio as a function of the normalized magnetic field for P5-15 M-SMP. (c) Mechanical stretch ratio as a function of the normalized magnetic field for P10-15 M-SMP. The magnetic field is normalized by the magnetization $|\mathbf{M}|$ and the characteristic stiffness μ_N at 85 °C.

4. Dynamic response of M-SMPs

In the following, we will present various examples to show the multifunctionalities of M-SMPs, including rapid and reversible deformation, selective/sequential actuation, and shape locking. To demonstrate the rapid and reversible deformation of M-SMP in response to magnetic actuation as well as to examine the effect of viscoelasticity on its dynamic behavior, in this section, the dynamic response of an M-SMP cantilever beam subjected to a uniform time-dependent actuation magnetic field under heating is studied through a combination of experiments and theoretical modeling.

4.1. Experiments

As shown in Fig. 4(a), we consider a straight cantilever beam of length L=20 mm, thickness t=0.75 mm, and width w=5 mm. The beam is made of P10-15 M-SMP with mass density $\rho=2.482$ g/cm³ and has a uniform magnetization $|\mathbf{M}|=88$ kA/m along the x-axis. An integrated electromagnetic coil system is used to heat and actuate the beam. The system, as shown in Fig. S4 in Supplementary Material, consists of a water-cooled solenoid for induction heating and two Helmholtz coils for generating a uniform actuation magnetic field. In the experiments, a uniform time-dependent actuation magnetic field with $|\mathbf{B}^a|=30\sin(2\pi ft)$ mT, is applied in the y-direction, and two different actuation frequencies are considered, i.e., f=0.25 and 1.0 Hz. Dynamic response and thermal images of the M-SMP beam under different actuation magnetic fields are demonstrated in **Video 1** in Supplementary Material (results associated with actuation frequencies 0.1 and 5 Hz are also presented).

4.2. Theoretical modeling

To better understand the dynamic behavior of the M-SMP beam, we develop a simplified beam model that can predict the transient response of the beam under a time-dependent actuation magnetic field. The beam is modeled as an inextensible Kirchhoff rod, which means that the stretching energy of the beam and the thermal expansion induced by the temperature change are neglected. Based on the Kirchhoff rod theory, without considering the effect of rotational inertia, the balance of linear and angular momenta gives (Plaut et al., 2008; Goriely, 2017; Kodio et al., 2020)

$$\frac{\partial \mathbf{F}_{b}}{\partial \mathbf{s}} + \mathbf{f} = \rho A \frac{\partial^{2} \mathbf{r}^{2}}{\partial t^{2}} + c \frac{\partial \mathbf{r}}{\partial t},\tag{19}$$

$$\frac{\partial \mathbf{M}_{b}}{\partial s} + \frac{\partial \mathbf{r}}{\partial s} \times \mathbf{F}_{b} + \mathbf{m} = \mathbf{0},\tag{20}$$

where $s \in [0, L]$ is the arc length coordinate, t is the time, ρ is the mass density, A is the cross-sectional area of the beam, and c is the viscosity. \mathbf{F}_b and \mathbf{M}_b are the resultant force and moment acting on the centerline of the beam, respectively, and $\mathbf{r} = x\mathbf{e}_1 + y\mathbf{e}_2 + z\mathbf{e}_3$ is the vector that describes the position of the centerline. Moreover, \mathbf{f} and \mathbf{m} are the body force and torque per unit reference length. Here, the body force and torque are induced by the applied actuation magnetic field. For a uniform magnetic field, the magnetic force vanishes, and the magnetic torque is given by (Zhao et al., 2019)

$$\mathbf{m} = \mathbf{M} \times \mathbf{B}^{\mathbf{a}}.\tag{21}$$

By using Eqs. (19)–(21), the governing equations for the dynamic analysis of an M-SMP beam with only in-plane deformation can be obtained as

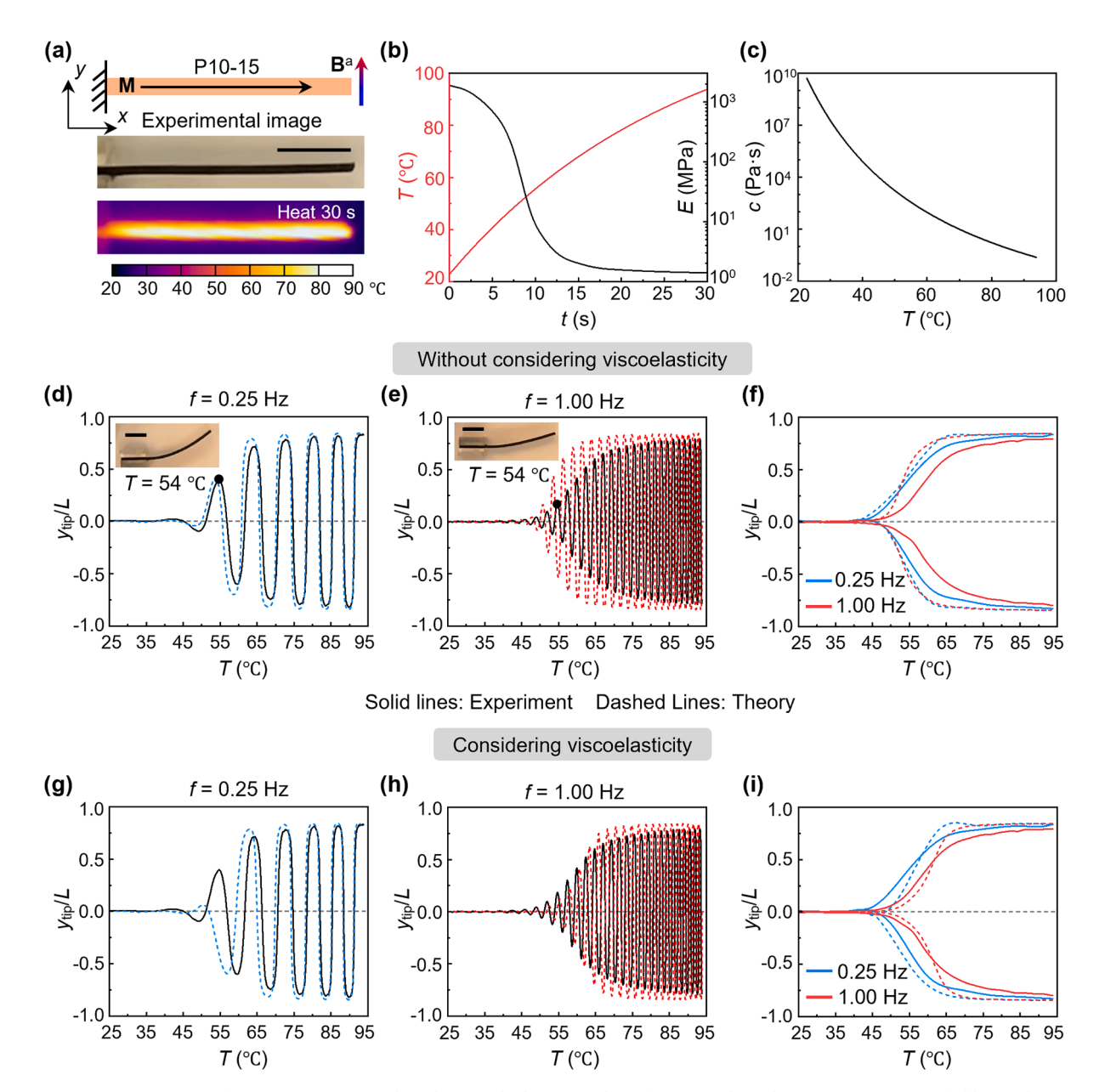


Fig. 4. Dynamic response of a P10-15 M-SMP cantilever beam under heating and a uniform time-dependent actuation magnetic field. (a) Schematic (top), experimental setup (middle), and thermal image (bottom) of the beam. (b) Temperature and Young's modulus variations of the beam during 30 s of heating. (c) Viscosity of the P10-15 M-SMP as a function of the temperature. (d–f) Comparison of the normalized experimental tip deflection of the cantilever beam subject to a magnetic field $|\mathbf{B}^a|=30\sin(2\pi ft)$ mT with that predicted by the beam model without considering viscoelasticity: (d) f=0.25 Hz, (e) f=1 Hz, and (f) normalized tip deflection envelopes. (g–i) Comparison of the normalized experimental tip deflection entitlever beam with that predicted by the beam model considering viscoelasticity: (g) f=0.25 Hz, (h) f=1 Hz, and (i) normalized tip deflection envelopes. Scale bars in (a), (d), and (e): 6 mm.

$$\frac{\partial F_{x}}{\partial s} = \rho A \frac{\partial^{2} x}{\partial t^{2}} + c \frac{\partial x}{\partial t},$$

$$\frac{\partial F_{y}}{\partial s} = \rho A \frac{\partial^{2} y}{\partial t^{2}} + c \frac{\partial y}{\partial t},$$

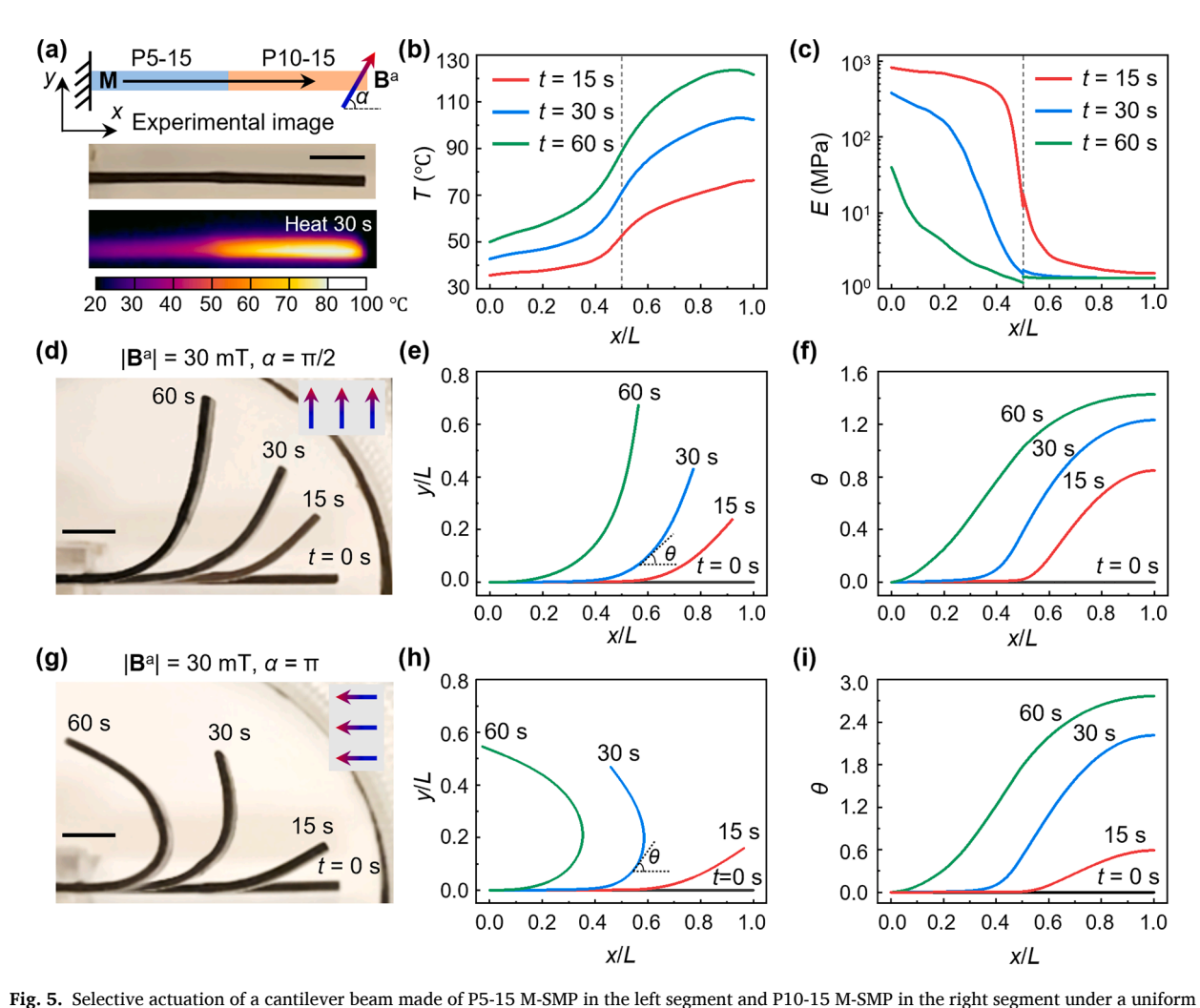
$$EI \frac{\partial \kappa}{\partial s} - |\mathbf{M}| |\mathbf{B}^{a}| A \sin(\theta - \alpha) = F_{x} \sin\theta - F_{y} \cos\theta,$$
(22)

with

$$\frac{\partial x}{\partial s} = \cos\theta, \frac{\partial y}{\partial s} = \sin\theta, \kappa = \frac{\partial\theta}{\partial s},\tag{23}$$

where θ is the bending angle between the centerline and the *x*-axis, α is the angle between the magnetic field and the *x*-axis, κ is the curvature, *E* is the Young's modulus, *I* is the second moment of area, and F_x and F_y are the force components along the *x* and *y* directions, respectively. For a cantilever beam, the initial and boundary conditions are given by

$$x(s,0) = 0, y(s,0) = 0, \theta(s,0) = 0,$$
 (24)

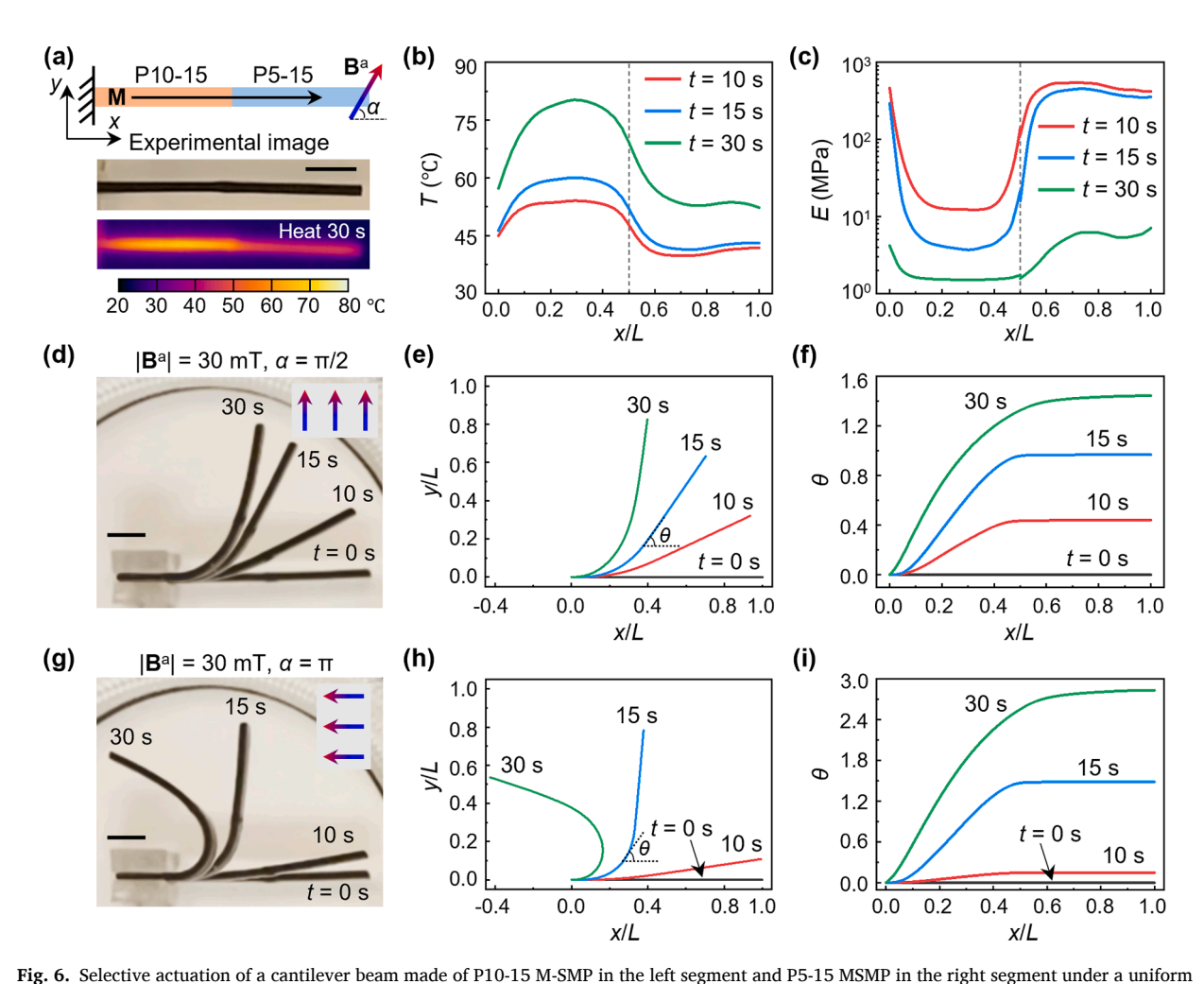


rig. 5. Selective actuation of a cantilever beam made of P5-15 Mr-SMP in the left segment and P10-15 Mr-SMP in the left segment and P10-15 Mr-SMP in the left segment under a uniform magnetic field and heating. (a) Schematic (top), experimental setup (middle) and thermal image (bottom) of the two-segment Mr-SMP cantilever beam. (b) Temperature profiles along the *x*-axis of the beam under heating for different times. (d) Experimental snapshots of the deformed configurations of the beam under a vertical magnetic field ($|\mathbf{B}^a|$ = 30 mT and $\alpha = \pi/2$) and heating for different times. (e, f) Theoretical predictions of the (e) deformed configurations and (f) bending angle (θ) along the axis of the beam. (g) Experimental snapshots of the deformed configurations of the beam under a horizontal magnetic field ($|\mathbf{B}^a|$ = 30 mT and $\alpha = \pi$) and heating for different times. (h, i) Theoretical predictions of the (h) deformed configurations and (i) bending angle (θ) along the axis of the beam. Scale bars in (a), (d), and (g): 4 mm.

$$x(0,t) = 0, y(0,t) = 0, \theta(0,t) = 0, \kappa(L,t) = 0.$$
 (25)

Eqs. (22)–(25) can be numerically solved using the finite difference method, and details are provided in **Appendix D**. Note that when dropping the time-dependent terms and setting $F_x = F_y = 0$, the dynamic beam model reduces to the static hard-magnetic elastica model in Wang et al. (2020). Additionally, both Young's modulus and viscosity of the M-SMP beam are temperature-dependent, and they vary with time t during heating. The temperature along the beam is considered uniform (see the thermal image in Fig. 4(a)), and its variation during 30 s of heating is recorded by a thermal camera, indicated by the red curve in Fig. 4(b). The Young's modulus of the beam during heating is interpolated from the experimentally measured Young's moduli of P10-15 M-SMP at various temperatures, depicted by the black curve in Fig. 4(b). The viscosity of the beam during heating is determined by fitting the measured storage modulus and loss tangent of P10-15 M-SMP using a generalized Maxwell model (see details in Section S3 and Fig. S5 in Supplementary Material).

Based on the theoretical model and experiments, the dynamic behavior of the M-SMP beam under heating and a uniform time-dependent magnetic field is studied. As shown in Fig. 4(b) and 4(c), the beam was heated from 22 to 95 °C in 30 s, during which the Young's modulus of the beam decreases from approximately 1800 to 1.4 MPa and the viscosity decreases from the order of 10^9 to 10^{-1} Pa•s. Experimental results for the normalized tip deflections (y_{tip}/L) of the M-SMP cantilever beam during heating and actuation are shown by the solid curves in Fig. 4(d) and 4(e) for the cases of f = 0.25 and 1 Hz, respectively. It is seen that when the temperature is approximately below 45 °C, the beam can hardly deform under the magnetic field due to the high elastic modulus of M-SMP in the



rig. 6. Selective actuation of a cantilever beam made of P10-15 M-SMP in the left segment and P5-15 MSMP in the left segment under a uniform magnetic field and heating. (a) Schematic (top), experimental setup (middle), and thermal image (bottom) of the two-segment M-SMP cantilever beam. (b) Temperature profiles along the *x*-axis of the beam under different heating times. (c) Young's modulus profiles along the *x*-axis of the beam under different heating times. (d) Experimental snapshots of the deformed configurations of the beam under a vertical magnetic field ($|\mathbf{B}^a| = 30 \text{ mT}$ and $\alpha = \pi/2$) and heating for different times. (e, f) Theoretical predictions of the (e) deformed configurations and (f) bending angle (θ) along the axis of the beam. (g) Experimental snapshots of the deformed configurations of the beam under a horizontal magnetic field ($|\mathbf{B}^a| = 30 \text{ mT}$ and $\alpha = \pi$) and heating for different times. (h, i) Theoretical predictions of the (h) deformed configurations and (i) bending angle (θ) along the axis of the beam. Scale bars in (a), (d), and (g): 4 mm.

glassy state. As the temperature increases, the SMPs in the beam gradually transition to the rubbery state. Consequently, the beam softens, and the maximum deflection increases. At around 75 °C, all the SMPs reach the rubbery state, and the maximum deflection saturates and remains unchanged with further increases in temperature. The beam oscillates with the alternating actuation magnetic field, revealing the rapid and reversible deformation capability of the M-SMP beam. When the M-SMP beam is actuated at the same temperature (e.g., 54 °C) under magnetic fields with the same magnitude but different frequencies, the deflections are different, as shown in the insets in Fig. 4(d) and 4(e).

To understand the role of viscoelasticity in the dynamic response of the M-SMP beam, Fig. 4(d–i) compare the theoretical predictions with the experimental results for the normalized tip deflection of the M-SMP beam under different actuation-frequency magnetic fields. Theoretical results with and without considering viscoelasticity are both presented. When the actuation frequency is relatively low (e.g., f = 0.25 Hz), the theoretical result without considering viscoelasticity agrees well with the experimental result

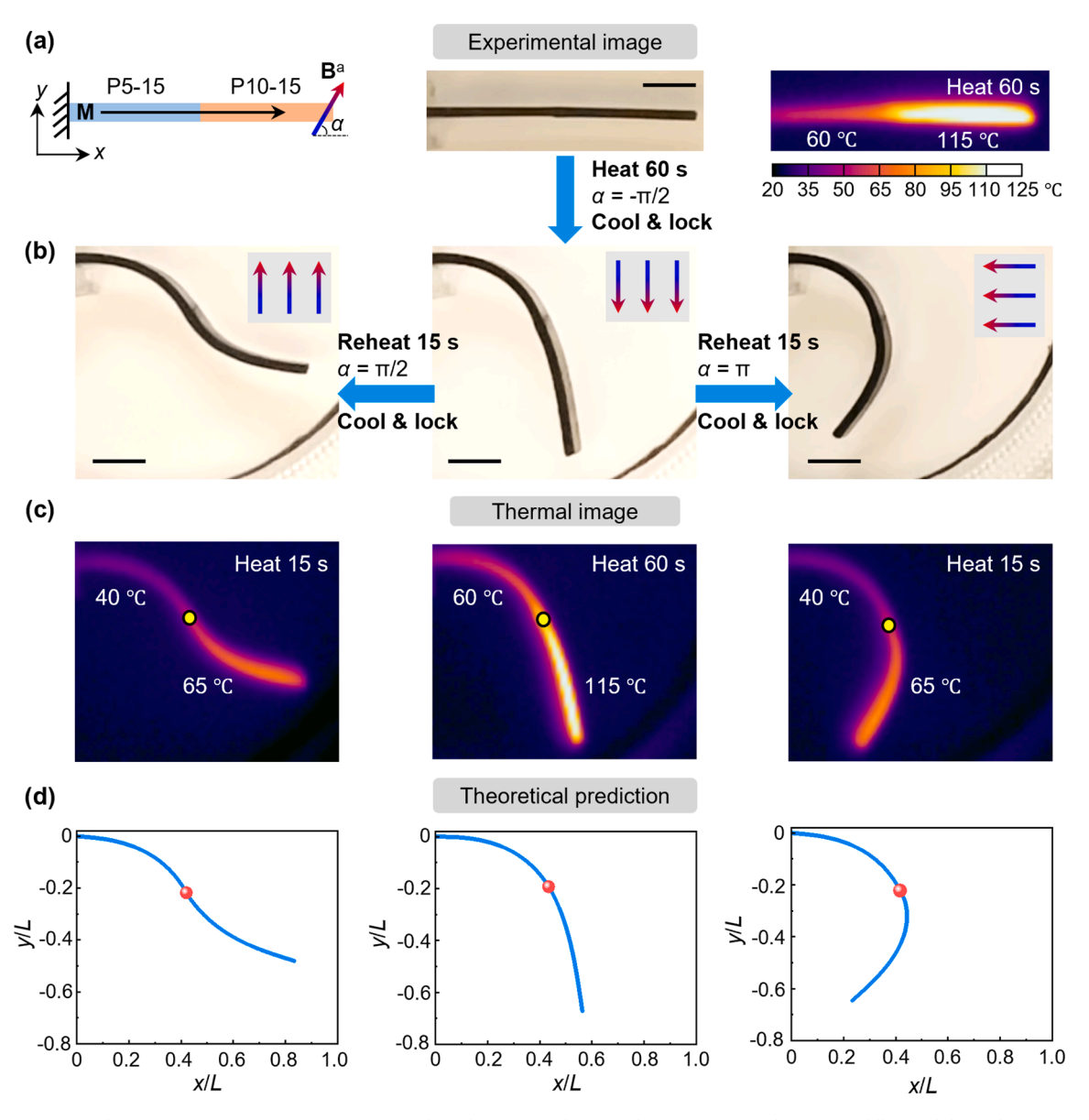


Fig. 7. Sequential actuation of a two-segment M-SMP cantilever beam. (a) Schematic (left), experimental image (middle), and thermal image (right) of an initially straight two-segment M-SMP cantilever beam. (b) Bending configurations of the initially straight beam under a downward magnetic field (middle) after heating for 60 s, the shape-locked beam under an upward magnetic field (left) after heating for 15 s, and the shape-locked beam under a leftward magnetic field (right) after heating for 15 s. (c) Thermal images of the three bending configurations in Fig. (b) after heating. (d) Bending configurations of the beam predicted by the theoretical model. Note that the temperature varies along the axis of the beam during heating, and the temperatures indicated in the thermal images correspond to the midpoint temperatures of each segment. The dots in Figs. (c) and (d) denote the midpoint of the beam where the two segments are connected. Scale bars in (a) and (b): 4 mm.

(Fig. 4(d)). However, the theoretical model incorporating viscoelasticity underestimates the tip deflection, especially at temperatures near $T_g = 53$ °C (Fig. 4(g)). This indicates that viscoelasticity has little effect on the dynamic response of M-SMP subjected to a magnetic field with low frequency. By contrast, at higher actuation frequency (e.g., f = 1 Hz), the theoretical model without considering viscoelasticity overestimates the tip deflection, especially at temperatures near T_g (Fig. 4(e)). As expected, when the viscoelasticity effect is incorporated into the theoretical model, the obtained result matches the experimental result well (Fig. 4(h)), which reveals that viscoelasticity plays a more important role in the dynamic behavior of M-SMP under high-frequency magnetic actuation. The comparisons also show that viscoelasticity tends to reduce the deformation of the M-SMP, as shown in Fig. 4(f) and 4(i), where the measured tip deflection of the cantilever beam at lower actuation frequency is slightly larger than at higher actuation frequency.

5. Static bending of M-SMPs

In this section, we investigate the static bending of two-segment cantilever beams made of M-SMPs with varying volume fractions of magnetic particles in the two segments, demonstrating the selective and sequential actuation of M-SMPs.

5.1. Experiments

As shown in Fig. 5(a), we fabricate a two-segment M-SMP cantilever beam, with the left segment made of P5-15 M-SMP and the right segment made of P10-15 M-SMP. The two segments have the same length of 10 mm, cross-sectional height of 0.75 mm, and width of 5 mm. Additionally, both segments have a magnetization of 88 kA/m along the *x*-axis. Under induction heating, the two segments exhibit different heating efficiencies and temperatures (see the thermal image in Fig. 5(a)). By controlling the heating time, and thereby the modulus, the two segments of the M-SMP beam can be selectively actuated. Here, we apply a static uniform magnetic field with $|\mathbf{B}^{\mathbf{a}}| = 30$ mT in either the vertical direction ($\alpha = \pi/2$) or horizontal direction ($\alpha = \pi$) to actuate the beam (see **Video 2** in Supplementary Material). For comparison purposes, in Fig. 6, we also consider a two-segment beam with its left segment made of P10-15 M-SMP and the right segment made of P5-15 M-SMP (see **Video 3** in Supplementary Material). Further, in Fig. 7, we demonstrate a two-segment M-SMP beam under two-step magnetic actuation (see **Video 4** in Supplementary Material).

5.2. Theoretical modeling

We first develop a simplified theoretical model to predict the large deformation of the two-segment M-SMP beam under magnetic loading. Here, the beam is also considered to be inextensible and unshearable during deformation. Thus, the elastic energy of the beam is only contributed by the bending deformation, which can be written as

$$U_{\text{bend}} = \frac{1}{2} \int_{0}^{L_{1}} E_{1} I_{1} (\kappa_{1} - \kappa_{0})^{2} ds + \frac{1}{2} \int_{L_{1}}^{L_{1}+L_{2}} E_{2} I_{2} (\kappa_{2} - \kappa_{0})^{2} ds$$

$$= \frac{1}{2} \int_{0}^{L_{1}} E_{1} I_{1} \left(\frac{d\theta_{1}}{ds} - \frac{d\theta_{0}}{ds} \right)^{2} ds + \frac{1}{2} \int_{L_{1}}^{L_{1}+L_{2}} E_{2} I_{2} \left(\frac{d\theta_{2}}{ds} - \frac{d\theta_{0}}{ds} \right)^{2} ds,$$
(26)

where E_i I_b L_b κ_b and θ_i (i=1 and 2) represent Young's modulus, second moment of area, length, curvature, and bending angle between the centerline and the x-axis, respectively, with i=1 corresponding to the left segment and i=2 representing the right segment. Moreover, κ_0 is the initial curvature and θ_0 is the initial angle between the centerline and the x-axis. For an initially straight beam, $\kappa_0 = \theta_0 = 0$. Further, according to Eq. (11), the magnetic potential energy of the two-segment beam is given by

$$U_{\text{mag}} = -\int_{0}^{L_{1}} |\mathbf{M}_{1}| |\mathbf{B}^{\text{a}}| A_{1} \cos(\theta_{1} - \alpha) ds - \int_{L_{1}}^{L_{1} + L_{2}} |\mathbf{M}_{2}| |\mathbf{B}^{\text{a}}| A_{2} \cos(\theta_{2} - \alpha) ds, \tag{27}$$

where $|\mathbf{M}_1|$ and $|\mathbf{M}_2|$ represent the magnetizations, and A_1 and A_2 denote the cross-sectional areas of the left and right segments, respectively.

By employing the principle of minimum potential, i.e., $\delta U_{\text{bend}} + \delta U_{\text{mag}} = 0$, the governing equation for the static analysis of the two-segment M-SMP beam under a uniform magnetic field can be obtained as

$$\begin{cases}
\frac{d}{ds} \left[E_1 I_1 \left(\frac{d\theta_1}{ds} - \frac{d\theta_0}{ds} \right) \right] - |\mathbf{M}_1| |\mathbf{B}^{\mathbf{a}}| A_1 \sin(\theta_1 - \alpha) = 0, 0 \le s < L_1; \\
\frac{d}{ds} \left[E_2 I_2 \left(\frac{d\theta_2}{ds} - \frac{d\theta_0}{ds} \right) \right] - |\mathbf{M}_2| |\mathbf{B}^{\mathbf{a}}| A_2 \sin(\theta_2 - \alpha) = 0, L_1 \le s \le L_1 + L_2.
\end{cases} \tag{28}$$

Correspondingly, the boundary conditions for a two-segment cantilever beam at the two ends (s = 0 and $L_1 + L_2$) and the joint ($s = L_1$) are given by

$$\theta_{1}(0) = 0, \frac{d\theta_{2}}{ds}|_{s=L_{1}+L_{2}} = \frac{d\theta_{0}}{ds}|_{s=L_{1}+L_{2}},$$

$$\theta_{1}(L_{1}) = \theta_{2}(L_{1}), E_{1}I_{1}\left(\frac{d\theta_{1}}{ds} - \frac{d\theta_{0}}{ds}\right)|_{s=L_{1}} = E_{2}I_{2}\left(\frac{d\theta_{2}}{ds} - \frac{d\theta_{0}}{ds}\right)|_{s=L_{1}}.$$
(29)

Eqs. (28) and (29) can be numerically solved using either the finite difference method or the ODE solver in MATLAB (see Section S4 in Supplementary Material for details), from which the bending deformation of a two-segment cantilever beam under a magnetic field can be obtained. In particular, the position coordinate (*x*, *y*) of the beam's centerline in the deformed configuration can be evaluated by

$$x(s) = \begin{cases} \int_0^s \cos\theta_1 ds, 0 \le s < L_1, \\ \int_0^{L_1} \cos\theta_1 ds + \int_{L_1}^s \cos\theta_2 ds, L_1 \le s \le L_1 + L_2. \end{cases}$$
 (30)

$$y(s) = \begin{cases} \int_0^s \sin\theta_1 ds, 0 \le s < L_1, \\ \int_0^{L_1} \sin\theta_1 ds + \int_{L_1}^s \sin\theta_2 ds, L_1 \le s \le L_1 + L_2. \end{cases}$$
 (31)

Based on the theoretical model and experiments, we study the bending deformation of the two-segment cantilever beam under a uniform magnetic field with different heating times. As shown in Fig. 5(a), when the left segment of the beam consists of P5-15 M-SMP and the right segment of the beam consists of P10-15 M-SMP, the temperature of the left segment is lower than the temperature of the right segment (see the thermal image) under heating. The measured temperature profiles along the beam axis under different heating times are shown in Fig. 5(b). It is seen that the temperature is non-uniformly distributed but gradually increases along the beam axis (at the tip end, the temperature slightly decreases). Consequently, the Young's modulus of the beam decreases along the beam axis (Fig. 5 (c)). For the heating time t = 30 and 60 s, the temperature of the right segment of the beam is much higher than the glass transition temperature, and thus its modulus remains nearly unchanged and is equal to the saturated modulus in the rubbery state. Moreover, at the joint of the two segments, the modulus of the right segment is slightly higher than the modulus of the left segment due to its higher magnetic particle volume fraction. Experimental snapshots of the deformed configurations of the two-segment beam under a vertical magnetic field ($\alpha = \pi/2$) after heating 15, 30, and 60 s are presented in Fig. 5(d), and the theoretically predicted bending configurations and bending angles are shown in Fig. 5(e) and 5(f). One can see that the theoretical predictions are in good agreement with the experimental results. When heating for 15 s, the left segment of the beam cannot be actuated and only the right segment deforms under the applied magnetic field. When heating for 30 s, the beam begins to deform near the fixed end (approximately 0.3L from the fixed end). After 60 s of heating, the entire beam becomes very soft and can be actuated from the fixed end. Fig. 5(g-i) illustrate the experimental images and the theoretical predictions of the two-segment beam under a horizontal magnetic field ($\alpha = \pi$) under heating for different times. Similarly, as the heating time and temperature increase, the length of the beam that can be actuated gradually increases, leading the beam to bend towards the direction of the applied magnetic field.

When flipping the positions of the two segments, namely, the left segment is composed of P10-15 M-SMP and the right segment is composed of P5-15 M-SMP, the bending behavior of the beam changes significantly. In this case, upon heating, the temperature of the right segment is lower than the left segment, as shown in the thermal image in Fig. 6(a). Temperature and Young's modulus profiles along the axis of the beam after heating for different times are presented in Fig. 6(b) and 6(c). It is seen that the temperature and Young's modulus vary along the beam axis. At the midpoint of the beam where the two segments are connected, Young's modulus of the left segment is slightly higher than that of the right segment. When applying a vertical magnetic field $(\alpha=\pi/2)$, the bending configuration of the beam mainly depends on the deformation of the left segment due to its lower Young's modulus (see Fig. 6(d) and 6 (e)). The right segment of beam barely deforms, and its bending angle is basically equal to the bending angle of the left segment at the joint (see Fig. 6(f)). When the direction of the applied magnetic field is horizontal $(\alpha=\pi)$, the static bending of the beam is still dominated by the left segment (see Fig. 6(g-i)). As can be seen, the deformation of the beam is relatively small after heating for 10 s. However, the deformation significantly increases and the right segment of the beam bends into a nearly vertical state after 15 s of heating (see Fig. 6(g) and 6(h)). This can be interpreted from Fig. 6(b) that when heating for 15 s, the temperature of the left segment reaches the glass transition temperature $(T_g=53\ ^{\circ}\text{C})$, at which a large amount of glassy phase of the M-SMP transitions into the rubbery phase and results in a rapid decrease of the modulus. Therefore, by rationally designing the magnetic particle volume fraction and actively controlling the heating temperature, the M-SMPs can be selectively actuated.

Next, we will show that by harnessing the shape-locking capability of SMPs, an M-SMP can be sequentially actuated, and its deformation can be reprogrammed by controlling the heating and actuation magnetic fields. As shown in Fig. 7(a), a two-segment beam made of P5-15 M-SMP in the left segment and P10-15 M-SMP in the right segment is considered. Upon heating, the temperature varies along the axis of the beam. After heating for 60 s, the temperatures at the middle points of the left and right segments are roughly 60 °C and 115 °C, respectively. When applying a downward magnetic field, the beam bends into a drooping arch shape (see the middle of Fig. 7(b)). After cooling to room temperature and removing the actuation magnetic field, the beam is locked in the deformed shape. Interestingly, the beam's deformation can be reprogrammed by reheating the shape-locked beam. As shown in Fig. 7(c), after reheating the beam for 15 s, the temperatures at the middle points of the two segments rise to about 40 °C and 65 °C, respectively, and thereby can be actuated by the applied magnetic field. For example, when the direction of the actuation magnetic field is upward, the

beam deforms into a half-wave shape (see the left of Fig. 7(b)). When the direction of the actuation magnetic field is leftward, the beam bends into a curved arch (see the right of Fig. 7(b)). Similarly, lowering the temperature of the beam can lock the actuated configurations. The various deformed configurations of the M-SMP beam can also be predicted using the simplified theoretical model Eq. (28). As shown in Fig. 7(d), the theoretical predictions of the deformed shapes of the beam match the experimental results very well. It is expected that by combining optimization algorithms (Lum et al., 2016; Wang et al., 2021), topology optimization (Zhao and Zhang, 2022), or machine learning techniques (Ma et al., 2022), the theoretical model can be used to find the magnetization, modulus profile, and magnetic field for achieving the inverse design of M-SMP beams that can deform into target configurations.

6. M-SMP origami

Finally, we present a demonstration to showcase the remarkable potential of M-SMPs in constructing origami structures with shapelocking and high load-carrying capabilities. Fig. 8(a) presents a schematic of the M-SMP origami hinge, where the panels are made of P0-30 M-SMP and the hinge is made of P10-15 M-SMP. Note that the P0-30 M-SMP does not contain Fe₃O₄ particles and thus cannot be induction heated. The hinge and the panels are magnetized along the direction (denoted by the black arrows) perpendicular to the hinge axis (denoted by the dashed line) with $|\mathbf{M}_1| = 88 \text{ kA/m}$ and $|\mathbf{M}_2| = 176 \text{ kA/m}$, respectively. The magnetization direction on the two sides of the hinge axis is opposite, such that a bending moment can be induced to fold the hinge when subjected to an out-of-plane magnetic field B^a. The folding behavior of such an M-SMP hinge can be evaluated using the two-segment beam model developed in Section 5 by taking one panel and half hinge for the analysis (see bottom of Fig. 8(a) and details on the implementation of the theoretical model are provided in Section S5 and Fig. S6 in Supplementary Material). Under induction heating, the panels remain unheated due to the absence of Fe₃O₄ particles while the hinge is heated to 80 °C within 60 s (Fig. 8(b)). The stiffness of the heated hinge significantly decreases which allows it to be actuated by a magnetic field $|\mathbf{B}^a| = 70 \text{ mT}$. The folded configuration of the M-SMP hinge predicted by the two-segment beam model is compared with the experimental result in Fig. 8(c) and the experimental folding process is presented in Video 5 in Supplementary Material. It is seen that the theoretical prediction matches the experimental results well. Assembling two such hinges, one can obtain a Miura origami (Miura-ori) unit (Schenk and Guest, 2013; Wei et al., 2013), as shown in Fig. 8(d). By rationally designing the magnetization directions in the panels and hinges (represented by the black arrows), the M-SMP Miura-ori can fold under magnetic actuation upon heating (Fig. 8(e) and 8(f) and Video 5 in Supplementary Material). After cooling, the Miura-ori locks its actuated shape without the application of the magnetic field. The shape-locking state exhibits a high load-carrying capacity owing to the high modulus of the M-SMP at room temperature. For the M-SMP Miura-ori we fabricate, it can support a weight of 50 grams, which is ten times its weight. This suggests that M-SMPs can serve as promising candidates for constructing origami structures with shape-locking and high load-carrying capabilities.

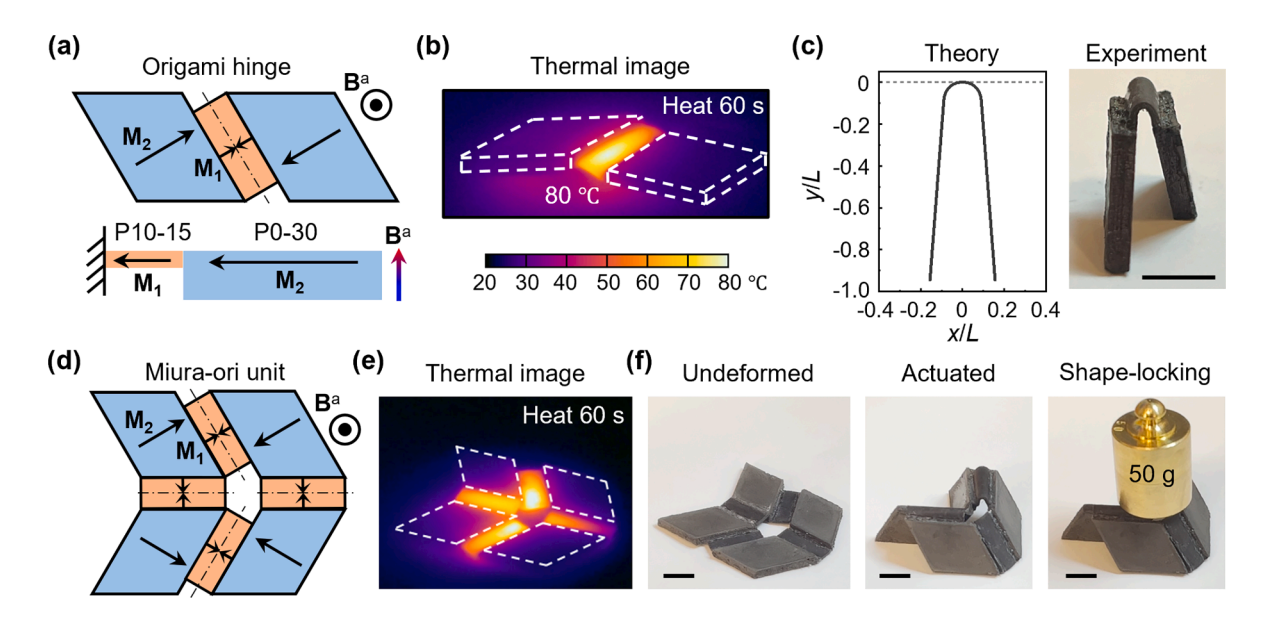


Fig. 8. M-SMP origami. (a) Schematic of an M-SMP origami hinge (top) whose one half can be equivalent to a two-segment cantilever beam (bottom). The panels are made of P0-30 M-SMP and the hinge is made of P10-15 M-SMP. The panels and the hinge have different thicknesses and magnetizations (denoted by black arrows). The dimensions of the origami hinge are provided in Fig. S6 in Supplementary Material. (b) Thermal image of the hinge upon heating for 60 s. (c) Folded configuration of the hinge under a uniform out-of-plane magnetic field obtained by theory and experiment. (d) Schematic of an M-SMP Miura-ori unit obtained by assembling two origami hinges in (a). (e) Thermal image of the Miura-ori upon heating for 60 s. (f) Undeformed, actuated, and shape-locking states of the Miura-ori under a uniform out-of-plane magnetic field. Scale bars in (c) and (f): 8 mm.

7. Conclusions

In this work, we have developed a constitutive model for M-SMPs based on the finite deformation theory. The behavior of M-SMPs in the rubbery state, dominated at high temperatures (above the glass transition temperature), is described by the Arruda-Boyce model, while the behavior of M-SMPs in the glassy state, dominated at low temperatures (below the glass transition temperature), is described by the neo-Hookean model and a nonlinear viscous flow rule. Moreover, the magneto-elastic behavior of M-SMPs is evaluated by accounting for the magnetic potential energy of the magnetic particles in response to an external actuation field. The material parameters in the model were calibrated by fitting the experimental results, which also showed that the developed model could predict the thermomechanical and magneto-elastic responses of M-SMPs at varying temperatures. To demonstrate the versatile functionalities of M-SMPs, we investigated the dynamic and static behaviors of various M-SMP cantilever beams, under magnetic fields and heating, through simplified beam models. The results indicate that M-SMPs can undergo rapid and reversible deformation in response to a timedependent magnetic field, while the dynamic response is dependent on the viscoelasticity. Specifically, viscoelasticity tends to reduce the deformation of M-SMPs, particularly near the glass transition temperature and under high-frequency magnetic actuation. Moreover, by designing the volume fraction of the magnetic particles and actively controlling the heating temperature, M-SMPs can be selectively or sequentially actuated. Upon cooling, the actuated shape of an M-SMP can be locked. The locked state has a high stiffness due to the high elastic modulus of M-SMP at low temperatures, which provides an ideal platform for constructing functional structures with shape-locking ability. For example, the origami structure made of M-SMPs can maintain its folded shape without external constraints and meanwhile possess high load-carrying capability. It is envisioned that the developed constitutive framework and simplified beam models can provide guidance for the design of M-SMPs and thus enable more functional applications.

CRediT authorship contribution statement

Lu Lu: Methodology, Software, Formal analysis, Visualization, Validation, Writing – original draft. **Shuai Wu:** Investigation, Formal analysis, Visualization, Validation, Writing – review & editing. **Ruike Renee Zhao:** Conceptualization, Validation, Project administration, Funding acquisition, Supervision, Writing – review & editing.

Declaration of competing interest

The authors declare that they have no known competing financial interests or personal relationships that could have appeared to influence the work reported in this paper.

Data availability

Data and code are available in the Supplementary Materials.

Acknowledgments

This work was supported by the National Science Foundation Career Award CMMI-2145601 and National Science Foundation Award CMMI-2142789.

Supplementary materials

Supplementary material associated with this article can be found, in the online version, at doi:10.1016/j.jmps.2024.105742.

Appendix A. Nominal stress under uniaxial tension

The M-SMP is considered to be nearly incompressible, which means that $J_{\text{me}} = 1$. In this case, the Cauchy stress can be obtained following the same process for compressible M-SMPs presented in Section 2, which is given by

$$\sigma = \underbrace{\frac{\mu_{\text{N}}}{3J_{\text{th}}} \frac{\lambda_{\text{L}}}{\bar{\lambda}_{\text{eff}}} \mathscr{L}^{-1} \left(\frac{\bar{\lambda}_{\text{eff}}}{\lambda_{\text{L}}} \right) \mathbf{B}_{\text{me}}}_{\sigma_{\text{neq}}} + \underbrace{\frac{\mu_{\text{neq}}}{J_{\text{th}}} \mathbf{B}_{\text{e}}}_{\sigma_{\text{neq}}} + \underbrace{\left(-\mathbf{B}^{\text{a}} \otimes \mathbf{M} \right)}_{\sigma_{\text{mag}}} - p\mathbf{I},$$
(A.1)

where p is the hydrostatic pressure that can be determined from boundary conditions. Under uniaxial tension, we assume that the mechanical load is applied in the \mathbf{e}_2 direction. Then, the mechanical part of the deformation gradient can be written as

$$\mathbf{F}_{me} = \frac{1}{\sqrt{\lambda_{me}}} \mathbf{e}_1 \otimes \mathbf{e}_1 + \lambda_{me} \mathbf{e}_2 \otimes \mathbf{e}_2 + \frac{1}{\sqrt{\lambda_{me}}} \mathbf{e}_3 \otimes \mathbf{e}_3, \tag{A.2}$$

where λ_{me} is the mechanical stretch ratio in the \mathbf{e}_2 direction. Thereby, the left Cauchy-Green tensor for \mathbf{F}_{me} is given by

$$\mathbf{B}_{\text{me}} = \mathbf{F}_{\text{me}} \mathbf{F}_{\text{me}}^{\text{T}} = \frac{1}{\lambda_{\text{me}}} \mathbf{e}_1 \otimes \mathbf{e}_1 + \lambda_{\text{me}}^2 \mathbf{e}_2 \otimes \mathbf{e}_2 + \frac{1}{\lambda_{\text{me}}} \mathbf{e}_3 \otimes \mathbf{e}_3. \tag{A.3}$$

By using Eqs. (A.1) and (A.3), the equilibrium part of the Cauchy stress can be obtained as

$$\boldsymbol{\sigma}_{eq} = \frac{\mu_{N}}{3J_{th}} \frac{\lambda_{L}}{\bar{\lambda}_{eff}} \mathcal{L}^{-1} \left(\frac{\bar{\lambda}_{eff}}{\lambda_{L}} \right) \boldsymbol{B}_{me} = \frac{\mu_{N}}{3J_{th}} \frac{\lambda_{L}}{\bar{\lambda}_{eff}} \mathcal{L}^{-1} \left(\frac{\bar{\lambda}_{eff}}{\lambda_{L}} \right) \left(\frac{1}{\lambda_{me}} \boldsymbol{e}_{1} \otimes \boldsymbol{e}_{1} + \lambda_{me}^{2} \boldsymbol{e}_{2} \otimes \boldsymbol{e}_{2} + \frac{1}{\lambda_{me}} \boldsymbol{e}_{3} \otimes \boldsymbol{e}_{3} \right). \tag{A.4}$$

Similarly, the elastic part of the deformation gradient under uniaxial tension can be written as

$$\mathbf{F}_{\mathrm{e}} = \frac{1}{\sqrt{\lambda_{\mathrm{e}}}} \mathbf{e}_{1} \otimes \mathbf{e}_{1} + \lambda_{\mathrm{e}} \mathbf{e}_{2} \otimes \mathbf{e}_{2} + \frac{1}{\sqrt{\lambda_{\mathrm{e}}}} \mathbf{e}_{3} \otimes \mathbf{e}_{3}, \tag{A.5}$$

where λ_e is the elastic stretch ratio. Then, the left Cauchy-Green tensor for \mathbf{F}_e is

$$\mathbf{B}_{e} = \mathbf{F}_{e} \mathbf{F}_{e}^{\mathrm{T}} = \frac{1}{\lambda_{e}} \mathbf{e}_{1} \otimes \mathbf{e}_{1} + \lambda_{e}^{2} \mathbf{e}_{2} \otimes \mathbf{e}_{2} + \frac{1}{\lambda_{e}} \mathbf{e}_{3} \otimes \mathbf{e}_{3}, \tag{A.6}$$

Substituting Eq. (A.6) into Eq. (A.1), the nonequilibrium part of the Cauchy stress can be obtained as

$$\boldsymbol{\sigma}_{\text{neq}} = \frac{\mu_{\text{neq}}}{J_{\text{th}}} \mathbf{B}_{\text{e}} = \frac{\mu_{\text{neq}}}{J_{\text{th}}} \left(\frac{1}{\lambda_{\text{e}}} \mathbf{e}_1 \otimes \mathbf{e}_1 + \lambda_{\text{e}}^2 \mathbf{e}_2 \otimes \mathbf{e}_2 + \frac{1}{\lambda_{\text{e}}} \mathbf{e}_3 \otimes \mathbf{e}_3 \right). \tag{A.7}$$

With Eqs. (A.1), (A.4), and (A.7), one can obtain the Cauchy stresses in the 3 principal directions under uniaxial tension as

$$\sigma_{11} = \sigma_{33} = \frac{\mu_{\rm N}}{3J_{\rm th}} \frac{\lambda_{\rm L}}{\lambda_{\rm eff}} \mathcal{L}^{-1} \left(\frac{\overline{\lambda}_{\rm eff}}{\lambda_{\rm L}}\right) \frac{1}{\lambda_{\rm me}} + \frac{\mu_{\rm neq}}{J_{\rm th}} \frac{1}{\lambda_{\rm e}} - p,\tag{A.8}$$

$$\sigma_{22} = \frac{\mu_{\rm N}}{3J_{\rm th}} \frac{\lambda_{\rm L}}{\lambda_{\rm off}} \mathcal{L}^{-1} \left(\frac{\bar{\lambda}_{\rm eff}}{\lambda_{\rm L}}\right) \lambda_{\rm me}^2 + \frac{\mu_{\rm neq}}{J_{\rm th}} \lambda_{\rm e}^2 - p. \tag{A.9}$$

If the material is unconstrained in e_1 and e_3 directions, one has $\sigma_{11} = \sigma_{33} = 0$. Then, subtracting Eq. (A.8) from Eq. (A.9) yields

$$\sigma_{22} = \frac{\mu_{\rm N}}{3J_{\rm th}} \frac{\lambda_{\rm L}}{\bar{\lambda}_{\rm eff}} \mathcal{J}^{-1} \left(\frac{\bar{\lambda}_{\rm eff}}{\lambda_{\rm L}} \right) \left(\lambda_{\rm me}^2 - \frac{1}{\lambda_{\rm me}} \right) + \frac{\mu_{\rm neq}}{J_{\rm th}} \left(\lambda_{\rm e}^2 - \frac{1}{\lambda_{\rm e}} \right). \tag{A.10}$$

To fit the nominal stress-strain curves measured in experiments, the Cauchy stress is transformed into the nominal stress through $N = J \mathbf{F}^{-1} \sigma$, where $J = J_{\text{th}}$ and

$$\mathbf{F} = \mathbf{F}_{\text{me}}\mathbf{F}_{\text{th}} = J_{\text{th}}^{1/3} \left(\frac{1}{\sqrt{\lambda_{\text{me}}}} \mathbf{e}_1 \otimes \mathbf{e}_1 + \lambda_{\text{me}} \mathbf{e}_2 \otimes \mathbf{e}_2 + \frac{1}{\sqrt{\lambda_{\text{me}}}} \mathbf{e}_3 \otimes \mathbf{e}_3 \right). \tag{A.11}$$

Thus, the nominal stress in the e_2 direction is given by

$$N_{22} = J_{\text{th}} J_{\text{th}}^{-1/3} \lambda_{\text{me}}^{-1} \sigma_{22} = \frac{\mu_{\text{N}}}{3 J_{\text{th}}^{1/3}} \frac{\lambda_{\text{L}}}{\bar{\lambda}_{\text{eff}}} \mathcal{L}^{-1} \left(\frac{\bar{\lambda}_{\text{eff}}}{\lambda_{\text{L}}} \right) \left(\lambda_{\text{me}} - \frac{1}{\lambda_{\text{me}}^2} \right) + \frac{\mu_{\text{neq}}}{J_{\text{th}}^{1/3} \lambda_{\text{me}}} \left(\lambda_{\text{e}}^2 - \frac{1}{\lambda_{\text{e}}} \right). \tag{A.12}$$

Appendix B. Viscous flow rule under uniaxial tension

Under uniaxial tension, the viscous part of the deformation gradient can be written as

$$\mathbf{F}_{\mathbf{v}} = \frac{1}{\sqrt{\lambda_{\mathbf{v}}}} \mathbf{e}_{1} \otimes \mathbf{e}_{1} + \lambda_{\mathbf{v}} \mathbf{e}_{2} \otimes \mathbf{e}_{2} + \frac{1}{\sqrt{\lambda_{\mathbf{v}}}} \mathbf{e}_{3} \otimes \mathbf{e}_{3}, \tag{A.13}$$

where λ_v is the viscous stretch ratio. Then, the velocity gradient and inverse of \mathbf{F}_v are given by

$$\begin{split} \dot{\mathbf{F}}_{v} &= -\frac{1}{2} (\lambda_{v})^{-3/2} \dot{\lambda}_{v} \mathbf{e}_{1} \otimes \mathbf{e}_{1} + \dot{\lambda}_{v} \mathbf{e}_{2} \otimes \mathbf{e}_{2} - \frac{1}{2} (\lambda_{v})^{-3/2} \dot{\lambda}_{v} \mathbf{e}_{3} \otimes \mathbf{e}_{3}, \\ \mathbf{F}_{v}^{-1} &= \sqrt{\lambda_{v}} \mathbf{e}_{1} \otimes \mathbf{e}_{1} + \frac{1}{\lambda_{v}} \mathbf{e}_{2} \otimes \mathbf{e}_{2} + \sqrt{\lambda_{v}} \mathbf{e}_{3} \otimes \mathbf{e}_{3}, \end{split} \tag{A.14}$$

which leads to

$$\mathbf{D}_{v} = \text{sym} \big(\dot{\mathbf{F}}_{v} \mathbf{F}_{v}^{-1} \big) = -\frac{1}{2} \frac{\dot{\lambda}_{v}}{\dot{\lambda}_{v}} (\mathbf{e}_{1} \otimes \mathbf{e}_{1} - 2\mathbf{e}_{2} \otimes \mathbf{e}_{2} + \mathbf{e}_{3} \otimes \mathbf{e}_{3}). \tag{A.15}$$

Moreover, the deviatoric part of the nonequilibrium component of the Cauchy stress can be obtained from Eq. (A.7) as

$$\boldsymbol{\sigma}_{\text{neq}}^{'} = \boldsymbol{\sigma}_{\text{neq}} - \frac{1}{3} \text{tr} (\boldsymbol{\sigma}_{\text{neq}}) \mathbf{I} = \frac{1}{3} \frac{\mu_{\text{neq}}}{J_{\text{th}}} \left(\frac{1}{\lambda_{e}} - \lambda_{e}^{2} \right) (\mathbf{e}_{1} \otimes \mathbf{e}_{1} - 2\mathbf{e}_{2} \otimes \mathbf{e}_{2} + \mathbf{e}_{3} \otimes \mathbf{e}_{3}), \tag{A.16}$$

and its norm is given by

$$\| \sigma_{\text{neq}}' \| = \frac{\sqrt{6}}{3} \frac{\mu_{\text{neq}}}{J_{\text{th}}} \left(\lambda_{\text{e}}^2 - \frac{1}{\lambda_{\text{e}}} \right). \tag{A.17}$$

Thus, we have

$$\mathbf{n} = \frac{\boldsymbol{\sigma}_{\text{neq}}'}{\parallel \boldsymbol{\sigma}_{\text{neq}}' \parallel} = -\frac{1}{\sqrt{6}} (\mathbf{e}_1 \otimes \mathbf{e}_1 - 2\mathbf{e}_2 \otimes \mathbf{e}_2 + \mathbf{e}_3 \otimes \mathbf{e}_3). \tag{A.18}$$

Substituting Eqs. (A.15) and (A.18) into Eq. (16) yields

$$\frac{\dot{\lambda}_{\rm v}}{\lambda_{\rm v}} = \frac{\sqrt{6}}{3} \dot{\gamma}_{\rm v}. \tag{A.19}$$

Based on Eqs. (17), (18), and (A.19), the viscous stretch ratio λ_v under uniaxial tension can be determined. Finally, using $\lambda_{me} = \lambda_v \lambda_e$, the evolution rule for the elastic stretch ratio can be identified.

Appendix C. Uniaxial magnetic actuation of a cube

Assuming that the directions of the magnetization M and magnetic field B^a are both along the e_2 -direction, then based on Eqs. (A.1), (A.2), and (A.5), the Cauchy stress in e_2 -direction of a nearly incompressible cube can be written as

$$\sigma_{22} = \frac{\mu_{\rm N}}{3J_{\rm th}} \frac{\lambda_{\rm L}}{\lambda_{\rm eff}} \mathcal{L}^{-1} \left(\frac{\hat{\lambda}_{\rm eff}}{\lambda_{\rm L}}\right) \lambda_{\rm me}^2 + \frac{\mu_{\rm neq}}{J_{\rm th}} \lambda_{\rm e}^2 - |\mathbf{B}^{\rm a}| |\mathbf{M}| \lambda_{\rm me} - p. \tag{A.20}$$

Cauchy stress in the other two principal directions have been given in Eq. (A.8). Considering the traction-free boundary condition, one has $\sigma_{11} = \sigma_{22} = \sigma_{33} = 0$. Subtracting Eq. (A.8) from Eq. (A.20), the relation between the applied magnetic field and the induced deformation can be determined by

$$\frac{\mu_{\rm N}}{3J_{\rm th}} \frac{\lambda_{\rm L}}{\bar{\lambda}_{\rm eff}} \mathcal{L}^{-1} \left(\frac{\bar{\lambda}_{\rm eff}}{\lambda_{\rm L}}\right) \left(\lambda_{\rm me} - \frac{1}{\lambda_{\rm me}^2}\right) + \frac{\mu_{\rm neq}}{J_{\rm th}\lambda_{\rm me}} \left(\lambda_{\rm e}^2 - \frac{1}{\lambda_{\rm e}}\right) = |\mathbf{B}^{\rm a}| |\mathbf{M}|. \tag{A.21}$$

Appendix D. Finite difference for the dynamic beam model

To solve the governing equations (22) and (23) for the dynamic beam model, finite difference method is employed to discretize the partial differential equation systems. In particular, the arc length s along the beam is discretized by $s_i = (i-1)\Delta s$, $i=1,2,\cdots,m+1$, where $m=L/\Delta s$ is the step number in the spatial domain. The time t is discretized by $t_j = (j-1)\Delta t$, $j=1,2,\cdots,n+1$, where $n=t_{\text{total}}/\Delta t$ is the step number in the time domain with t_{total} being the total time. By employing the central differences, the discretized forms of Eqs. (22) and (23) are given by

$$\begin{split} \frac{x_{i+1,j} - x_{i,j}}{\Delta s} &= \cos\theta_{i+1/2,j}, \frac{y_{i+1,j} - y_{i,j}}{\Delta s} = \sin\theta_{i+1/2,j}, \frac{\theta_{i+1,j} - \theta_{i,j}}{\Delta s} = \kappa_{i+1/2,j}, \\ E_{i,j} I \frac{\kappa_{i+1,j} - \kappa_{i,j}}{\Delta s} &= |\mathbf{M}| \left| \mathbf{B}_{i,j}^{\mathbf{a}} \left| A \sin\left(\theta_{i+1/2,j} - \alpha_{i,j}\right) = F_{i+1/2,j}^{\mathbf{x}} \sin\theta_{i+1/2,j} - F_{i+1/2,j}^{\mathbf{y}} \cos\theta_{i+1/2,j}, \\ \frac{F_{i+1,j}^{\mathbf{x}} - F_{i,j}^{\mathbf{x}}}{\Delta s} &= \rho A \frac{x_{i,j+1} - 2x_{i,j} + x_{i,j-1}}{\Delta t^2} + c_{i,j} \frac{x_{i,j+1} - x_{i,j}}{\Delta t}, \\ \frac{F_{i+1,j}^{\mathbf{y}} - F_{i,j}^{\mathbf{y}}}{\Delta s} &= \rho A \frac{y_{i,j+1} - 2y_{i,j} + y_{i,j-1}}{\Delta t^2} + c_{i,j} \frac{y_{i,j+1} - y_{i,j}}{\Delta t}. \end{split}$$
(A.22)

Note that $f_{i+1/2} = (f_i + f_{i+1})/2$, where f denotes the quantities θ , κ , F_x , and F_y . Moreover, the discretized versions of the initial and boundary conditions are written as

$$\begin{array}{l} x_{i,1} = 0, y_{i,1} = 0, \theta_{i,1} = 0, \\ x_{1j} = 0, y_{1j} = 0, \theta_{1j} = 0, \kappa_{m+1j} = 0. \end{array} \tag{A.23}$$

When giving the values of the variables at s_1 and t_1 , the system can be solved using various numerical iteration methods or optimization methods. In the present work, the optimization toolbox in MATLAB is employed to find the solutions. To reduce the optimization variables, the bending angle $\theta_{i,i}$ and the curvature $\kappa_{i,i}$ are assumed to have the following forms,

$$\theta_{i,j} = \sin\left(\frac{\pi s_{i}}{2L}\right) q_{j}^{(1)} + \sin\left(\frac{3\pi s_{i}}{2L}\right) q_{j}^{(2)} + \sin\left(\frac{5\pi s_{i}}{2L}\right) q_{j}^{(3)},$$

$$\kappa_{i,j} = \frac{\pi}{2L} \cos\left(\frac{\pi s_{i}}{2L}\right) q_{j}^{(1)} + \frac{3\pi}{2L} \cos\left(\frac{3\pi s_{i}}{2L}\right) q_{j}^{(2)} + \frac{5\pi}{2L} \cos\left(\frac{5\pi s_{i}}{2L}\right) q_{j}^{(3)}.$$
(A.24)

It is evident that Eq. (A.24) automatically satisfies the boundary conditions $\theta_{1,j}=0$ and $\kappa_{m+1,j}=0$. Therefore, we only need to optimize the coefficients $\left(q_j^{(1)},q_j^{(2)},q_j^{(3)}\right)$ in the time domain to satisfy the governing equations and boundary conditions. In the optimization, the step numbers m and n are designated as 20 and 360, respectively, for generating the results corresponding to the actuation frequency f=0.25 Hz in Fig. 4. For the results corresponding to the actuation frequency f=1 Hz, the step numbers are adjusted to 20 and 400.

References

Alapan, Y., Karacakol, A.C., Guzelhan, S.N., Isik, I., Sitti, M., 2020. Reprogrammable shape morphing of magnetic soft machines. Sci. Adv. 6, eabc6414.

Arruda, E.M., Boyce, M.C., 1993. A three-dimensional constitutive model for the large stretch behavior of rubber elastic materials. J. Mech. Phys. Solids 41, 389–412.

Boyce, M.C., Parks, D.M., Argon, A.S., 1988. Large inelastic deformation of glassy polymers. Part I: rate dependent constitutive model. Mech. Mater. 7, 15–33.

Boyce, M.C., Parks, D.M., Argon, A.S., 1989. Plastic flow in oriented glassy polymers. Int. J. Plast. 5, 593–615. Chen, T., Pauly, M., Reis, P.M., 2021. A reprogrammable mechanical metamaterial with stable memory. Nature 589, 386–390.

Cui, J., Huang, T.Y., Luo, Z., Testa, P., Gu, H., Chen, X.Z., Nelson, B.J., Heyderman, L.J., 2019. Nanomagnetic encoding of shape-morphing micromachines. Nature 575, 164–168.

Eyring, H., 1936. Viscosity, plasticity, and diffusion as examples of absolute reaction rates. J. Chem. Phys. 4, 283-291.

Ferry, J.D., 1980. Viscoelastic Properties of Polymers. John Wiley & Sons.

Goriely, A., 2017. The Mathematics and Mechanics of Biological Growth. Springer.

Hu, W., Lum, G.Z., Mastrangeli, M., Sitti, M., 2018. Small-scale soft-bodied robot with multimodal locomotion. Nature 554, 81-85.

Kim, Y., Yuk, H., Zhao, R., Chester, S.A., Zhao, X., 2018. Printing ferromagnetic domains for untethered fast-transforming soft materials. Nature 558, 274–279.

Kodio, O., Goriely, A., Vella, D., 2020. Dynamic buckling of an inextensible elastic ring: linear and nonlinear analyses. Phys.Rev. E 101, 053002.

Leanza, S., Wu, S., Sun, X., Qi, H.J., Zhao, R.R., 2024. Active materials for functional origami. Adv. Mater. 36, 2302066.
Li, G., Xu, W., 2011. Thermomechanical behavior of thermoset shape memory polymer programmed by cold-compression: testing and constitutive modeling. J. Mech. Phys. Solids 59, 1231–1250.

Li, Y., He, Y., Liu, Z., 2017. A viscoelastic constitutive model for shape memory polymers based on multiplicative decompositions of the deformation gradient. Int. J. Plast. 91, 300–317.

Lu, L., Sim, J., Zhao, R.R., 2024. Mechanics of hard-magnetic soft materials: a review. Mech. Mater. 189, 104874.

Lum, G.Z., Ye, Z., Dong, X., Marvi, H., Erin, O., Hu, W., Sitti, M., 2016. Shape-programmable magnetic soft matter. Proc. Natl. Acad. Sci. 113, E6007–E6015. Ma, C., Chang, Y., Wu, S., Zhao, R.R., 2022. Deep learning-accelerated designs of tunable magneto-mechanical metamaterials. ACS Appl. Mater. Interfaces 14, 33802–33902

Ma, C., Wu, S., Ze, Q., Kuang, X., Zhang, R., Qi, H.J., Zhao, R., 2021. Magnetic multimaterial printing for multimodal shape transformation with tunable properties and shiftable mechanical behaviors. ACS Appl. Mater. Interfaces 13, 12639–12648.

Montgomery, S.M., Wu, S., Kuang, X., Armstrong, C.D., Zemelka, C., Ze, Q., Zhang, R., Zhao, R., Qi, H.J., 2021. Magneto-mechanical metamaterials with widely tunable mechanical properties and acoustic bandgaps. Adv. Funct. Mater. 31, 2005319.

Nguyen, T.D., Qi, H.J., Castro, F., Long, K.N., 2008. A thermoviscoelastic model for amorphous shape memory polymers: incorporating structural and stress relaxation. J. Mech. Phys. Solids 56, 2792–2814.

Novelino, L.S., Ze, Q., Wu, S., Paulino, G.H., Zhao, R., 2020. Untethered control of functional origami microrobots with distributed actuation. Proc. Natl. Acad. Sci. 117, 24096–24101.

Plaut, R., Favor, H., Jeffers, A., Virgin, L., 2008. Vibration isolation using buckled or pre-bent columns–part 1: two-dimensional motions of horizontal rigid bar. J. Sound Vib. 310, 409–420.

Qi, H.J., Nguyen, T.D., Castro, F., Yakacki, C.M., Shandas, R., 2008. Finite deformation thermo-mechanical behavior of thermally induced shape memory polymers. J. Mech. Phys. Solids 56, 1730–1751.

Schenk, M., Guest, S.D., 2013. Geometry of Miura-folded metamaterials. Proc. Natl. Acad. Sci. 110, 3276-3281.

Sim, J., Wu, S., Dai, J., Zhao, R.R., 2023. Magneto-mechanical bilayer metamaterial with global area-preserving density tunability for acoustic wave regulation. Adv. Mater. 35, 2303541.

Sim, J., Zhao, R.R., 2024. Magneto-mechanical metamaterials: a perspective. J. Appl. Mech. 91, 031004.

Stewart, E.M., Anand, L., 2023. Magneto-viscoelasticity of hard-magnetic soft-elastomers: application to modeling the dynamic snap-through behavior of a bistable arch. J. Mech. Phys. Solids. 105366.

Wang, L., Chang, Y., Wu, S., Zhao, R.R., Chen, W., 2023. Physics-aware differentiable design of magnetically actuated kirigami for shape morphing. Nat. Commun. 14, 8516.

Wang, L., Kim, Y., Guo, C.F., Zhao, X., 2020. Hard-magnetic elastica. J. Mech. Phys. Solids 142, 104045.

Wang, L., Zheng, D., Harker, P., Patel, A.B., Guo, C.F., Zhao, X., 2021. Evolutionary design of magnetic soft continuum robots. Proc. Natl. Acad. Sci. 118, e2021922118.

Wei, Z.Y., Guo, Z.V., Dudte, L., Liang, H.Y., Mahadevan, L., 2013. Geometric mechanics of periodic pleated origami. Phys. Rev. Lett. 110, 215501.

Westbrook, K.K., Kao, P.H., Castro, F., Ding, Y., Qi, H.J., 2011. A 3D finite deformation constitutive model for amorphous shape memory polymers: a multi-branch modeling approach for nonequilibrium relaxation processes. Mech. Mater. 43, 853–869.

Wu, S., Eichenberger, J., Dai, J., Chang, Y., Ghalichechian, N., Zhao, R.R., 2022. Magnetically actuated reconfigurable metamaterials as conformal electromagnetic filters. Adv. Intell. Syst. 4, 2200106.

Wu, S., Ze, Q., Dai, J., Udipi, N., Paulino, G.H., Zhao, R., 2021. Stretchable origami robotic arm with omnidirectional bending and twisting. Proc. Natl. Acad. Sci. 118, e2110023118.

Xiao, R., Choi, J., Lakhera, N., Yakacki, C.M., Frick, C.P., Nguyen, T.D., 2013. Modeling the glass transition of amorphous networks for shape-memory behavior. J. Mech. Phys. Solids 61, 1612–1635.

Yu, K., Li, H., McClung, A.J., Tandon, G.P., Baur, J.W., Qi, H.J., 2016. Cyclic behaviors of amorphous shape memory polymers. Soft Matter 12, 3234–3245.

Ze, Q., Kuang, X., Wu, S., Wong, J., Montgomery, S.M., Zhang, R., Kovitz, J.M., Yang, F., Qi, H.J., Zhao, R., 2020. Magnetic shape memory polymers with integrated multifunctional shape manipulation. Adv. Mater. 32, 1906657.

Ze, Q., Wu, S., Dai, J., Leanza, S., Ikeda, G., Yang, P.C., Iaccarino, G., Zhao, R.R., 2022. Spinning-enabled wireless amphibious origami millirobot. Nat. Commun. 13, 3118.

Zeng, H., Leng, J., Gu, J., Sun, H., 2018. A thermoviscoelastic model incorporated with uncoupled structural and stress relaxation mechanisms for amorphous shape memory polymers. Mech. Mater. 124, 18–25.

Zeng, H., Song, L., Sun, H., Gu, J., Li, Z., 2023. A thermoviscoelastic model for the one-way and two-way shape memory effects of semi-crystalline polymers. Int. J. Eng. Sci. 185, 103830.

Zhao, R., Kim, Y., Chester, S.A., Sharma, P., Zhao, X., 2019. Mechanics of hard-magnetic soft materials. J. Mech. Phys. Solids 124, 244–263. Zhao, W., Li, N., Liu, L., Leng, J., Liu, Y., 2023a. Mechanical behaviors and applications of shape memory polymer and its composites. Appl. Phys. Rev. 10, 011306. Zhao, W., Liu, L., Lan, X., Leng, J., Liu, Y., 2023b. Thermomechanical constitutive models of shape memory polymers and their composites. Appl. Mech. Rev. 75,

Zhao, Z., Zhang, X.S., 2022. Topology optimization of hard-magnetic soft materials. J. Mech. Phys. Solids 158, 104628.